

Review

Self assembled monolayers on silicon for molecular electronics

D.K. Aswal^{a,b,*}, S. Lenfant^a, D. Guerin^a, J.V. Yakhmi^b, D. Vuillaume^a^a *Institut d'Electronique, Microelectronique et Nanotechnologie – CNRS “Molecular Nanostructures & Devices” group BP60069, avenue Poincare, F-59652 cedex, Villeneuve d'Ascq, France*^b *Technical Physics and Prototype Engineering Division, Bhabha Atomic Research Center, Trombay, Mumbai 400 085, India*

Received 13 July 2005; received in revised form 8 October 2005; accepted 13 October 2005

Available online 5 December 2005

Abstract

We present an overview of various aspects of the self-assembly of organic monolayers on silicon substrates for molecular electronics applications. Different chemical strategies employed for grafting the self-assembled monolayers (SAMs) of alkanes having different chain lengths on native oxide of Si or on bare Si have been reviewed. The utility of different characterization techniques in determination of the thickness, molecular ordering and orientation, surface coverage, growth kinetics and chemical composition of the SAMs has been discussed by choosing appropriate examples. The metal counterelectrodes are an integral part of SAMs for measuring their electrical properties as well as using them for molecular electronic devices. A brief discussion on the variety of options available for the deposition of metal counterelectrodes, that is, soft metal contacts, vapor deposition and soft lithography, has been presented. Various theoretical models, namely, tunneling (direct and Fowler–Nordheim), thermionic emission, Poole–Frenkel emission and hopping conduction, used for explaining the electronic transport in dielectric SAMs have been outlined and, some experimental data on alkane SAMs have been analyzed using these models. It has been found that short alkyl chains show excellent agreement with tunneling models; while more experimental data on long alkyl chains are required to understand their transport mechanism(s). Finally, the concepts and realization of various molecular electronic components, that is, diodes, resonant tunnel diodes, memories and transistors, based on appropriate architecture of SAMs comprising of alkyl chains (σ -molecule) and conjugated molecules (π -molecule) have been presented. © 2005 Elsevier B.V. All rights reserved.

Keywords: Self-assembled monolayers; Molecular electronics; Electronic transport

Contents

1.	Introduction	85
1.1.	Current trends in microelectronics	85
1.2.	Emergence of molecular electronics and current status	85
2.	Deposition of SAMs	87
2.1.	Basics of SAMs	87
2.2.	SAMs on native silicon oxide	87
2.2.1.	Reactive SiO ₂ surface precursors	87
2.2.2.	SAM formation	88
2.3.	SAMs directly on bare Si	89
2.3.1.	Reactive Si surface precursors	89
2.3.2.	SAM formation	90
3.	Characterization of SAMs	90
3.1.	Thickness of monolayer	90
3.2.	Molecular orientation and ordering	91
3.3.	Uniformity and coverage	92

* Corresponding author. Tel.: +91 22 25503134; fax: +91 22 25503134.

E-mail address: dkaswal@yahoo.com (D.K. Aswal).

3.3.1.	Wetting measurements	92
3.3.2.	Atomic force microscopy	93
3.3.3.	Electrochemical	94
3.4.	Chemical composition	94
3.5.	Thermal and chemical stability	95
4.	Metal counterelectrodes on SAMs	95
4.1.	Liquid Hg contacts	95
4.2.	Vacuum deposition	95
4.3.	Soft lithography	96
5.	Electronic conduction in SAMs	96
5.1.	Theoretical models	96
5.1.1.	Tunneling	96
5.1.2.	Thermionic emission	98
5.1.3.	Poole–Frenkel emission	98
5.1.4.	Hopping conduction	98
5.2.	Tunneling in short alkyl chains	98
5.3.	Length dependent electrical properties	100
5.4.	Dielectric breakdown of SAMs	101
6.	Molecular devices	101
6.1.	Molecular diodes	101
6.1.1.	Basic concepts	101
6.1.2.	Chemical synthesis	102
6.1.3.	Rectifying characteristics	103
6.2.	Molecular resonant tunnel diode (MRTD)	104
6.2.1.	Concept of MRTD	104
6.2.2.	Synthesis and characteristics of MRTD	104
6.3.	Molecular memories	105
6.4.	Molecular transistors	105
7.	Concluding remarks	106
	Acknowledgements	106
	References	106

1. Introduction

1.1. Current trends in microelectronics

Microelectronics, which was born about 50 years ago, has grown to a mature industry and is responsible for driving most of modern technology in today's world [1]. Semiconducting materials such as silicon, germanium, gallium–arsenide, etc. are the basic building blocks of the microelectronics industry. At present this industry is driven by two distinct forces:

- (i) *The development of new applications.* The technology based on microelectronics industry has already changed the lifestyle of the human race. One can find microelectronics playing a visible role in almost all fields, viz. automobiles, home appliances, telecommunications, medical and scientific equipments, etc. The industry keeps on identifying new areas of applications with additional features. For instance, the small portable phone that can be accommodated in the fist not only acts as a still and video camera, sends and receives email or surfs the Internet but also is in a position to control home appliances from any part of the world.
- (ii) *The miniaturization of existing ones.* The process of miniaturization means reducing the size of a device smaller and smaller and to make it work faster while keeping the price nearly constant. A classic example of this is the develop-

ment of computers: the performance increases several-folds in 1–2 years time while the price remains nearly same.

The concept of miniaturization is governed by the “Moore's law”, which suggests that the number of transistors on a chip would double every 18 months [2]. As the projected sizes of the transistors go down to 20 nm or below it, the end of “Moore's law” is being predicted. This is because below this size, the physics of the transistors lead to unacceptable power dissipation. In addition, at present the technology based on lithography to fabricate devices of this small size does not exist.

1.2. Emergence of molecular electronics and current status

As the total transistor size comes down to few nanometers—implying that only few atoms would work as a transistor—a shift in paradigm for the manufacture and integration of microelectronics components becomes apparent. And that signals the emergence of “molecular electronics” whereby one is looking for the design of an individual molecule or group of molecules that have a specific electronic functionality. Organic molecules—owing to their size, mechanical flexibility and chemical tenability—fit well in this slot and, thus are expected to play a key role in molecular electronics. The electrical properties of organic monolayers were first measured by Mann and Kuhn in 1971 [3]. This work also led to the development of an ordered

monolayer deposition of organic molecules via “self-assembly” through formation of chemical bonds between molecules and substrate [4,5]. Not forgetting, the most popular Langmuir and Blodgett (LB) technique for making organic monolayers was discovered in 1920, but the molecules–substrate bonds in this case is through physisorption and are thus weaker [6,7]. The first theoretical concept of using a single organic molecule as a rectifier was proposed by Aviram and Ratner in 1974 [8]. They showed that if one could couple a readily oxidizing group (D) to a readily reducing group (A), the alignment of the lowest unoccupied molecular orbital (LUMO) and highest occupied molecular orbital (HOMO) would be such that electronic conduction would be easier in one direction than the other, which results in a molecular diode. Subsequently, several device ideas were proposed based on the molecular logic structures [9]. In spite of the availability of these experimental abilities and theoretical ideas at that time, work on molecular electronics was not taken up seriously because the limitations on Si-based microelectronics, as discussed above, were not felt as strong at that time as one feels now and, the techniques that can image the molecules and manipulate them were not available. With the discovery of scanning probe microscope (SPM) by Binnig and Rohrer in 1981 [10,11], the work on molecular electronics took an upswing as using SPM not only we can see and manipulate organic molecules but also can measure their electrical properties. At present we are at the initial growth stage of “molecular electronics” where the emphasis is largely on synthesizing new organic molecules with different electronic functionalities and, on devising new methods to measure the electrical properties of the “single molecule” or a “group of molecules”. The methods employed mainly for the measurement of electronic transport in organic molecules so far are:

- (i) *Break-junction method* [12–14]. The method consists of the fabrication of a thin (<100 nm) metal line which is broken either by mechanical or electrical means. This results in a wire with a sub-nanometer size gap that can be spanned by one or a few molecules. The mechanical break junction is considered better as it allows a controlled change in the inter-electrode distance. The electromigration break junction, though simple to produce, are usually not identical.
- (ii) *Cross wire method* [15]. In this method, SAM is deposited on an Au wire (10 μm) and then a second Au wire (without SAM) is brought in close proximity to this wire. These wires are placed in a magnetic field and a current is forced through the unmodified wire. These results in a Laplace force pushing the unmodified wire towards the SAM coated wire. Eventually contact is established and the I – V characteristics of the SAM can be measured.
- (iii) *Metal nano-particles method* [16]. The metal nano-particles on which a SAM has been deposited are trapped between two closely spaced metal contacts using an alternating electric field.
- (iv) *Conductive probe atomic force microscope (CP-AFM) and scanning tunneling microscope (STM) method* [17–20]. In this method, a conducting AFM tip or STM tip is placed in proximity with a monolayer previously assembled on a conductive substrate.

- (v) *Nano-pore method* [21–23]. In this method, the molecules are sandwiched between two metal layers through a small orifice or nano-pore. A low stress and low conductivity Si_3N_4 film is grown on a Si wafer. Certain areas of the wafer are then etched away so as to leave free standing Si_3N_4 films. A pore of sub-50 nm diameter is then etched through these films. Au is then evaporated on the bottom of the wafer. A SAM is then assembled from the other side of the membrane on the Au surface exposed by the pore. Finally a top metal contact is evaporated onto the monolayer at reduced temperature.
- (vi) *Planar sandwich geometry*. In this case, metal counterelectrodes are directly fabricated on self assembled monolayers (SAMs) deposited on conducting substrates. The counterelectrode could be Hg-drop, vacuum evaporated Al or Au thin film or Au transfer by soft-lithography process. The electron transport in organic molecules has been reviewed by Saloman et al. [24].

Working with “planar sandwich geometry” is considered advantageous for molecular electronic applications as one can deposit $\sim 10^{15}$ molecules/ cm^2 , and conveniently fabricate two- and/or three-terminal molecular devices by choosing appropriate electrode configurations. At present, two types of SAMs are generally grown:

- (i) *Alkanethiol monolayers on gold substrates*. The first gold-alkylthiolate monolayer was produced by Allara and Nuzzo at Bell laboratories in 1983 [25]. They realized the utility of combining a relatively inert gold surface with a bifunctional organic molecule in well-ordered, regularly oriented array. Good review articles describing different aspects of alkanethiol monolayers on gold substrates are available in literature [26–30].
- (ii) *Attachment of organic molecules to SiO_2/Si or Si substrates via self-assembly process*. The formation of self-assembled organic monolayers on oxidized silicon surface from the solution of alkyltrichlorosilane was introduced by Bigelow et al. [31] and developed further by Maoz and Sagiv [32]. Our group has been working for the last several years on the SAMs on SiO_2/Si or Si substrates [33–47] as it has distinct additional advantages, viz. the possibility of designing new class of resonant tunneling devices owing to an energy gap offered by Si [48], and the availability of inputs from an already existing powerful silicon-based IC industry that can be used effectively for the development of integrated molecular devices or hybrid devices.

In this review, we cover various aspects of SAMs on SiO_2/Si or Si. The article is organized as follows. In Section 2, we review the methods to deposit SAMs on SiO_2/Si or Si substrates. The characterization of SAMs is presented in Section 3. A brief summary on the various methods of making metal counterelectrodes on SAMs is discussed in Section 4. The theoretical and experimental review on the electronic transport in SAMs is summarized in Section 5. A discussion comprising the concepts and realization of various molecular electronic devices,

viz. diode, resonant tunnel diode, memory and transistor, is presented in Section 6. The concluding remarks on the perspective of molecular electronics are presented in Section 7. Instead of citing all the work reported in the literature, we have attempted to generalize the ideas and concepts in this review and, occasionally suggested or speculated about the factors which we feel need further investigations. In the process we may have missed some important references. It is hoped that this review will provide an overview and thus stimulate the researchers to think about the opportunities and challenges in the molecular electronics.

2. Deposition of SAMs

2.1. Basics of SAMs

A schematic of organic SAM deposited on Si substrate suitable for molecular electronics is shown in Fig. 1. Usually, the SAMs are formed spontaneously by immersing the Si substrates into an active solution, e.g. surfactant molecules $R(CH_2)_nSiX_3$ ($X = Cl, OCH_3$ or OC_2H_5) dissolved in alkane/carbon tetrachloride. However, the SAMs can be deposited by other techniques as well, such as, vapor deposition. The self-assembling molecule can be divided into three parts:

- (i) *Head group, i.e. $-SiX_3$.* Forms the chemical bond with surface atoms of the substrate (exothermic: ~ 40 – 45 kcal/mol or ~ 1.7 eV) causing the pinning of surfactant molecule to the substrate.
- (ii) *Alkyl chain, i.e. $-(CH_2)_n-$.* The inter-chain van der Waals interactions (exothermic < 10 kcal/mol or < 0.4 eV) could assist in formation of ordered molecular structure which, of course, depends on the pinning density of the head groups.
- (iii) *Surface group, i.e. $-R$.* This is the terminal group which is replaced with different functional groups to obtain molecular electronics devices (discussed in Section 6).

A thin metal-layer (usually Al, Au or Hg-drop) is used on the top of the SAMs in order to measure their electrical properties and to fabricate molecular devices using them. A discussion on different metallization schemes is provided in the Section 4.

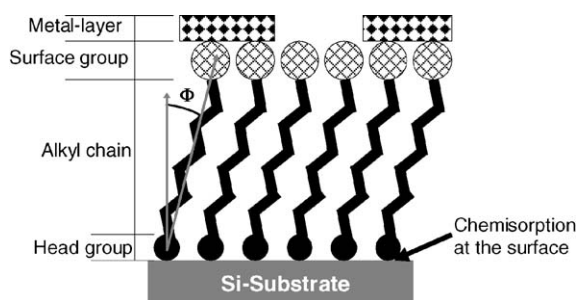


Fig. 1. A schematic diagram showing different parts of a self-assembled monolayer deposited on a Si-substrate suitable for molecular electronics. Φ is the tilt of the chain axis from the surface normal.

For a high density of head groups chemisorbed at the surface of the substrate—implying a good surface coverage—the alkyl chains become closer. Therefore, the interchain van der Waals interactions become effective, which leads to formation of a close-packed “ordered” or “solid-like” state (as schematically shown in Fig. 1). The alkyl chains, depending upon the surface coverage, have a tilt (Φ) from the surface normal. Usually higher the packing density, lower is the Φ . On the other hand, if the surface coverage is poor, the alkyl chains form a “disordered” or “liquid-like” state, and the Φ could be very large.

The commercially available single crystals of Si usually have a layer of native oxide (about 1–1.5 nm thickness), which forms on exposure to ambient atmosphere. Thus, for deposition of organic SAMs on Si two alternate strategies have been employed:

- (i) Deposition of SAMs on native silicon oxide by “silanization” or “vapor deposition”.
- (ii) Direct deposition of SAMs on silicon through Si–C bond formation.

2.2. SAMs on native silicon oxide

The native oxide layer usually contains a high density of traps therefore, it is desirable to remove the native oxide layer and grow an ultra-thin (1–1.5 nm) thermal oxide layer of better electrical quality. On a silicon oxide surface, three classes of molecules, namely, silanes ($RSiX_3$, with $X = Cl, OMe, OEt$), organometallics (RLi or $RMgX$), and alcohols (ROH) are widely used for the formation of self assembled monolayers. Thorough cleaning of the substrate is a prerequisite for obtaining a clean oxide layer with high density of silanol groups ($Si-OH$) on the surface. These silanol groups, which provide a highly hydrophilic surface (allowing molecules to diffuse on the physisorbed ultra-thin water layer), are either used as anchoring sites for silanization reactions or converted into more reactive functions (i.e. $Si-Cl$ or $Si-NEt_2$) suitable for alkylation or alkoxylation reactions.

2.2.1. Reactive SiO_2 surface precursors

Two methods are mainly used to obtain clean and hydroxylated thin oxide layer on silicon surface. The conventional RCA cleaning process, as described in Fig. 2 (method A), is still widely employed [49,50]. Many variations in the chemical sequence and, in the proportions of the reagents, have been used in the industry. RCA cleaning is achieved by dipping the Si wafer successively in a mixture of concentrated sulfuric acid and hydrogen peroxide, and then in an alkaline mixture of de-ionized (DI) water, ammonium hydroxide and hydrogen peroxide. These first two steps remove organic and inorganic contaminants as well as unwanted particulates (dust, silica, silicon, metals) from the wafer. Afterwards, surface SiO_2 layer is removed using dilute hydrofluoric acid. This step eliminates metal ions that may have diffused in silicon oxide during the first steps. Finally, pure native oxide is formed by treating the wafer in a bath of hydrochloric acid and hydrogen peroxide. This last step affords hydroxylated surface. Each cleaning step is approximately 10 min long and

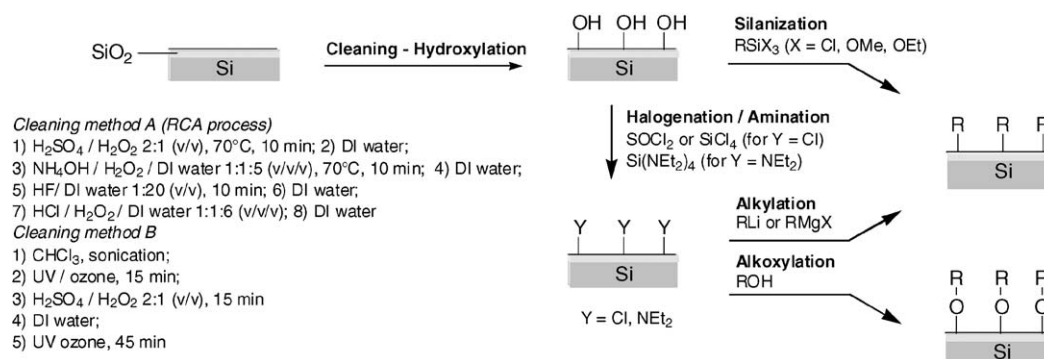


Fig. 2. Processes of the SAM formation on a native silicon oxide surface of Si.

is followed by thorough rinsing in DI water then drying under nitrogen.

Alternatively, hydroxylation is often accomplished following method B (as described in Fig. 2) in five steps [51–53]: (i) Sonication in chloroform to degrease and remove organic contamination; (ii) Photochemical precleaning by UV radiation in an oxygen atmosphere for 15 min to transform organic compounds, like hydrocarbons and oils, into gases or water-soluble species such as fatty acids; (iii) Piranha cleaning for ~10 min, i.e. immersion of the silicon wafers into a freshly prepared mixture of sulfuric acid and hydrogen peroxide. Basic medium of ammonia and hydrogen peroxide can also be used; (iv) thorough rinsing with DI water; and (v) finally, a further dry photochemical oxidation for ~45 min to remove the last traces of contaminants.

Both cleaning methods yield a density of $\sim 10^{15}$ $-\text{OH}$ groups/ cm^2 , and thus, in principle, one can chemisorb same density of organic molecules at the silicon surface. Dry etching by oxygen plasma is also an efficient technique frequently used to clean and hydroxylate silicon surfaces [54]. Halogenation or amination of hydroxylated surface make reactions of SiO_2 layer with alcohols, lithium compounds or Grignard reagents. Chloro-terminated SiO_2 is obtained by treatment either (i) with thionyl chloride in tetrahydrofuran, [55] or (ii) with tetrachlorosilane in toluene [56] or in the presence of pyridine under vacuum [57,58]. Amino-terminated surface are prepared by reaction of hydroxylated surface with aminosilane $\text{Si}(\text{NEt}_2)_4$ in dry toluene [58]. These reactions are air-sensitive, and thus must be conducted under inert atmosphere in strictly anhydrous medium. All the activated surfaces, i.e. $-\text{OH}$, $-\text{Cl}$ and $-\text{NEt}_2$, must be used immediately for preparation of SAMs.

2.2.2. SAM formation

Typically, freshly prepared hydroxylated surface are dipped into a reaction bath containing silane solution for the chemisorption of silane molecules on the hydroxylated Si surface [5–7,37–44,51–53]. The reaction bath is usually a 10^{-3} M solution of silane (RSiX_3 ; where X = Cl, OCH_3 or OC_2H_5) in alkane solvent such as dicyclohexyl or *n*-hexane. Addition in the medium of a fraction of CCl_4 favors the solubility of polar end group $-\text{SiX}_3$ of the silane molecule. Due to their water sensitiveness, trichlorosilanes or trialkoxysilanes are incorporated at the last moment under inert atmosphere to avoid their

polymerization in the medium. The temperature of the reaction bath is usually kept at temperatures between -30°C to room temperature, depending upon the length of alkyl chain, to form an ordered monolayer. Usually smaller the chain length, lower is the temperature required for formation of an ordered monolayer. For instance, the formation temperature of a chain having 10 carbon atoms is 0°C , while it is 38°C for 22 carbon chain [51]. The formation time for the monolayer using trichlorosilane molecules is about 1 h, while for trimethoxysilane or triethoxysilane molecules the monolayer formation takes about 2 days. It may be noted that the selection of a proper solvent is important. For instance, while hexane or heptane solvent results in the formation of compact high-quality octadecyltrichlorosilane monolayers; dodecane causes formation of multilayered films [59].

Silanes, particularly with short chain lengths and having high vapor pressures, are deposited in vapor phase on the substrate by evaporating pure molecule either under argon flow at room temperature [60,61], or by heating in confined medium, or under vacuum [33].

The mechanism of SAM formation during silanization process is depicted in Fig. 3, which takes place in four steps [52,53]. The first step is physisorption, in which the silane molecules get physisorbed at the hydrated silicon surface. In the second step the silane head-groups arriving close to the substrate hydrolyse—in the presence of the adsorbed water layer on the surface—into highly polar trihydroxysilane $-\text{Si}(\text{OH})_3$. These polar $-\text{Si}(\text{OH})_3$ groups form covalent bonds with the hydroxyl groups on SiO_2 surface (third step) subsequently to which condensation reaction goes on between silanol functions of neighbor molecules. Self-assembly is driven by lipophilic interactions between the linear alkane moieties. During initial period, only a few molecules will adsorb (by steps 1–3) on the surface and the monolayer will definitely be in a disordered (or liquid) state. However, at longer times, the surface coverage eventually reaches the point where a well-ordered and compact (or crystalline) monolayer is obtained (step 4). The kinetics of the monolayer formation can be investigated by the atomic force microscopy and other techniques and, a discussion on this aspect is presented in Section 3.3.

Halogenated or aminated surfaces react easily with organolithium (RLi) or organomagnesium compounds (RMgX) forming densely packed films through formation of $\text{Si}-\text{R}$ bond. On the other hand, treatment of activated SiO_2 with alcohols (ROH)

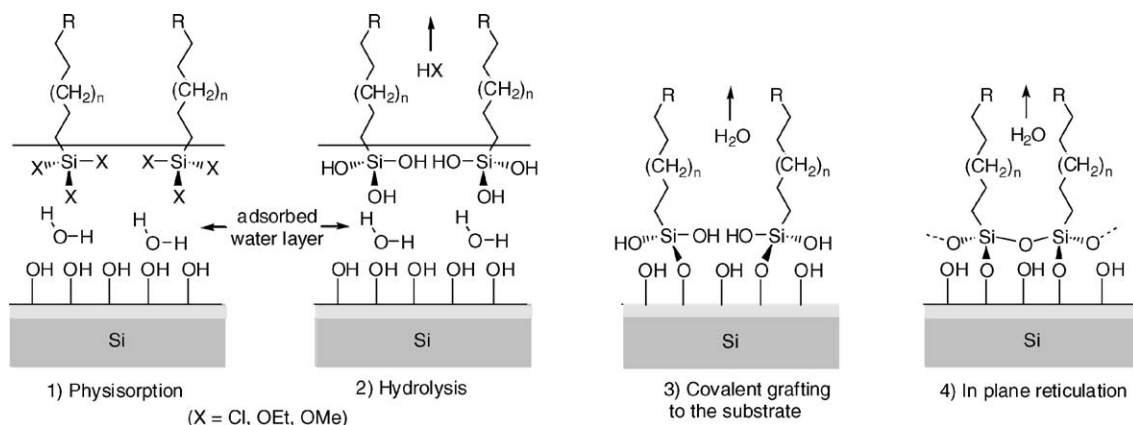


Fig. 3. Schematic showing different steps involved in the mechanism of SAM formation on a hydrated silicon surface.

provide alkoxyated surface through formation of Si–OR bonds. However, Si–O bond is more sensitive to solvolysis than Si–C bond in particular in boiling solvents such as water or methanol.

2.3. SAMs directly on bare Si

For certain investigations pertaining to molecular electronics applications, the presence of native oxide layer between organic molecule and Si might cause some hindrance, e.g. to study an interface between the organics and Si. Thus, in order to deposit organic SAMs directly on the Si following two steps are necessary, (i) complete removal of the native oxide layer and obtain a reactive surface precursor and (ii) formation of organic SAMs on the freshly prepared reactive surface precursor by making Si–C or Si–O bonds. The organic fictionalization of Si surfaces has been extensively reviewed elsewhere [62,63].

2.3.1. Reactive Si surface precursors

There are three known strategies to obtain a reactive Si surface precursor namely, (i) hydrogen-terminated Si, (ii) halogen-terminated Si and (iii) reconstructed Si surface.

To obtain H-terminated Si surface two etching processes are employed and are shown in Fig. 4 [64,65]. Treatment of (1 0 0) Si wafers with 1–2% HF (aqueous) produces atomically flat dihydride terminated Si surfaces ($\equiv\text{SiH}_2$). The (1 1 1) Si wafer treated with 40% NH_4F (aqueous) produces monohydride terminated Si surfaces ($\equiv\text{Si-H}$). The H-terminated Si surfaces are stable in air for few tens of minutes only and get oxidized if exposed for longer time.

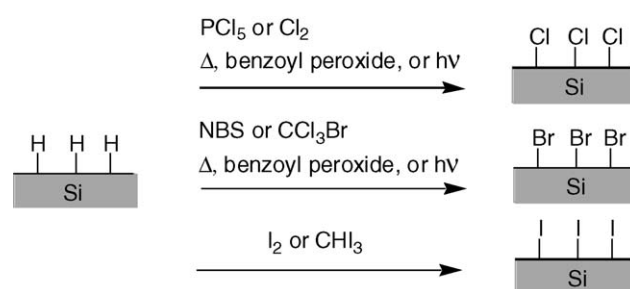


Fig. 5. Common methods used for silicon halogenations.

Different methods employed to obtain halogen terminated Si surface are presented in Fig. 5. The Chloro-terminated Si surfaces are prepared by treating the H-terminated Si (1 1 1) with PCl_5 at 80–100 °C using benzoyl peroxide as a radical initiator in chlorobenzene [66,67]. The other methods include (i) boiling Si wafer in chlorobenzene with PCl_5 and UV irradiation, and (ii) heating H-terminated Si at 80 °C in the presence of Cb [68]. Recently, high quality of halogenated silicon surfaces has been produced using gas phase reactions of hydrogenated silicon with molecular chlorine or bromine at room temperature [69]. Bromo-terminated Si surfaces can also be obtained by treating the H-terminated Si surface with CCl_3Br at 80 °C under UV irradiation. Bromination of Si–H surface is also performed sometime using an etching mixture made of HF, HNO_3 , $\text{CH}_3\text{CO}_2\text{H}$, Br_2 and KBr [70], but this method causes morphology changes of silicon surface [71]. Iodine [72,73] or iodoform [74] have also been used as iodinating agents to generate Si–I

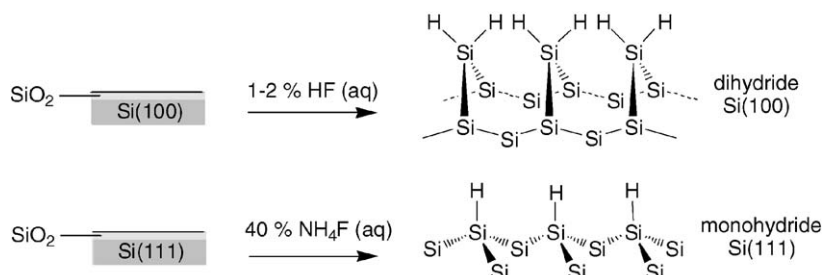


Fig. 4. Chemical etching processes to obtain H-terminated Si surface.

surface from hydrogenated silicon. The halogen-terminated surfaces are very reactive and thus need to be handled only under inert atmosphere.

Highly reactive bare silicon (1 0 0) and (1 1 1) surfaces can be obtained by heating the Si wafers at temperatures $>700^\circ\text{C}$ under ultra high-vacuum (UHV) conditions ($>10^{-10}$ Torr). Both the (1 0 0) and (1 1 1) Si surfaces undergo extensive reconstructions, i.e. their surface atomic geometry differs significantly from that of the bulk. However, the two surfaces have markedly different surface structures [75,76]. The Si (1 0 0) surface reconstructs into a (2×1) structure, forming pairs of silicon atoms known as dimers. On the other hand, Si (1 1 1) surface, reconstructs into a complex (7×7) structure that contains 49 surface atoms in the new unit cell.

2.3.2. SAM formation

Once the reactive Si surfaces are obtained, then the organic SAM can be formed on the surface by appropriate chemistry. Linford and Chidsey, in 1993, showed for the first time that organic molecules having an unsaturated bond can be grafted on the hydrogen-terminated Si by hydrosilylation reaction [77]. The alkyl monolayers have been prepared by inserting 1-alkenes into Si–H groups in the presence of diacyl peroxide radical initiator at 100°C . The proposed mechanism of monolayer formation is based on a series of free radical reactions, and is depicted in the Fig. 6 [78]. In the first step, the initiator, diacyl peroxide, breaks homolytically to form two acyloxy radicals, which eventually break apart to form an alkyl radical and carbon dioxide. In the second step, the alkyl radical abstracts the hydrogen atom from the hydrogen-terminated Si surface to produce silicon radical. In the final step, the silicon radical reacts with alkenes to form a Si–C bond. In a similar way, alkenyl monolayers can be grafted using alkyne molecules.

It has been found that at temperatures $>150^\circ\text{C}$, the Si–H bond undergoes a homolytic cleavage, $\text{Si–H} \rightarrow \text{Si}^\bullet + \text{H}^\bullet$, and yields a silicon radical at the surface, which then can react with alkenes, as described above. This process has been termed as “thermally induced hydrosilylation” [79,80]. The hydrosilylation process has also been promoted by UV irradiation known as “photochemical hydrosilylation” [81,82]. In addition, the organic monolayers have been grafted on the H-terminated Si surfaces using electrochemical methods [83].

Similar to the alkanes, as discussed in Section 2.2.2, alkyl or aryl monolayers have been grafted on activated Si (i.e. Si–H, Si–Cl, Si–Br, or Si–I surface) by using reactions with organomagnesium, organolithium or alcohols compounds, as shown in Fig. 7 [84,85].

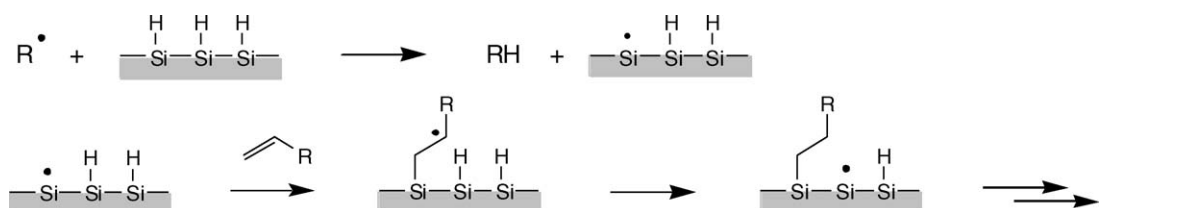


Fig. 6. Mechanism of hydrosilylation of olefins on hydrogenated silicon.

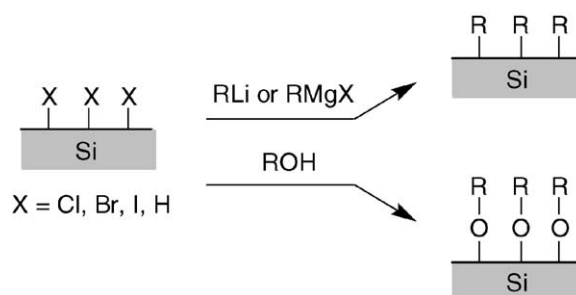


Fig. 7. Formation of monolayers on halogen terminated Si using organomagnesium, organolithium or alcohols.

A vast amount of work on the UHV functionalized (2×1) reconstructed Si surface exists in literature [63]. It is well established that the small unsaturated hydrocarbons such as ethylene, propylene, benzene, etc., get chemisorbed at (2×1) reconstructed Si surface via a $[2 + 2]$ cycloaddition reaction, as shown in Fig. 8 [86–89].

In the very recent time, scanning tunneling microscope (STM) tip has been used to modify the Si surface [90,91]. For instance, the Si–H bonds are broken by application of a tunneling current that leads to Si radical at the surface and to which alkenes are attached. However, this technique does not yield a comprehensive coverage of monolayers as the organic molecules are attached to only those places where Si radicals are formed.

3. Characterization of SAMs

The quality of deposited SAMs is assessed by characterizing them for (i) thickness of the monolayer, (ii) molecular orientation and ordering, (iii) uniformity and coverage, (iv) chemical composition, and (v) thermal and chemical stability of the monolayer. Various techniques for the characterization of monolayers are reviewed elsewhere [9,92].

3.1. Thickness of monolayer

Optical ellipsometry [93] is the most routinely used technique to determine the thickness of the SAMs, though other techniques, such as, plasmon surface polarization [94], X-ray reflectivity [95], X-ray standing waves [96], etc. can also be employed. In fact, one can theoretically determine the length of all trans-extended *n*-alkane chains by using MOPAC software or by simply adding the bond lengths. As discussed in the Section 2.2.2, the homologous series of methyl-terminated *n*-alkylsiloxane monolayers ($n=1-18$) have been routinely deposited by reaction between *n*-alkyltrichlorosilanes on native

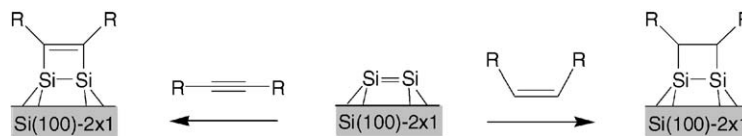


Fig. 8. [2 + 2] cycloaddition reactions of alkene and alkyne on a (2 × 1) reconstructed Si surface.

oxide of silicon. In this case, for all *trans*-extended chains, the length (t) of the monolayer containing n carbons (for CH₃ terminating monolayer) or $(n - 1)$ CH₂ units should have a linear relation:

$$t = 1.26 \times (n - 1) \times \cos \Phi + 4.78 \quad (1)$$

where Φ is the tilt angle of the chain, 1.26 Å (per methylene group) corresponds to the projection of carbon–carbon bond on to the main axis of the molecule, and the intercept of 4.78 is a sum of Si–O (1.33 Å), C–Si (1.52 Å) and length of terminating –CH₃ group (1.93 Å). In Fig. 9, along with this theoretical relation at different Φ , we have plotted the experimentally measured thickness of several n -alkylsiloxane monolayers by different groups [37,52,53]. It also may be noted, as shown in the inset of Fig. 9, that the deposition temperature of the monolayer (T_c) decreases with decreasing n [51]. It is evident that the bracket of experimental values is within the theoretical one with $\Phi < 30^\circ$. This implies that the methyl-terminated n -alkylsiloxane monolayers are deposited in all-*trans* conformation with a tilt angle of $< 30^\circ$ on native oxide of Si. However, the most studied $n = 18$ (i.e. octadecylsiloxane) SAMs is known to exhibit a tilt angle of $< 10^\circ$ [37,97].

Similarly, the theoretical thickness of alkyl chains deposited on H-terminated Si surface is given by

$$t = 1.26 \times (n - 1) \times \cos \Phi + 1.86 \quad (2)$$

where n is the number of C atoms in the alkene chain and 1.26 and 1.86 Å are respectively the C–C and Si–C bond lengths projected along the molecular axis. A comparison of experimental data [34,77,78,98,99], as shown in Fig. 10, makes it very evident

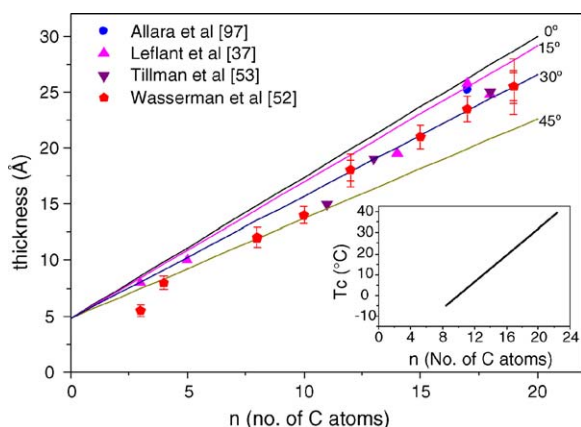


Fig. 9. Thickness of n -alkylsiloxane monolayers deposited on native-oxide of Si measured by different groups. The full lines are the theoretical relation of thickness as a function of n , calculated using Eq. (1) at different tilt angles. The inset shows the variation of the critical deposition temperature of monolayer (T_c) as a function of n [51].

that the alkyl monolayers deposited on H-terminated Si are tilted in the range 30 – 45° for $n > 10$ and, $> 45^\circ$ for $n < 10$. These tilt angles are slightly higher than those of alkylsiloxane monolayers deposited on native-oxide of Si, indicating a better surface coverage of the latter ones.

A molecular modeling simulation is an important way of finding the information on the structure of alkyl monolayers on the H-terminated Si (1 1 1) surface [100]. The effects of different substitution percentages (33.3, 50, 66.7 and 100%) of the Si–H for Si-alkyl groups on the monolayer structure showed that only with a substitution percentage of 50%, the structures obtained from molecular modeling and the available experimental data matches well. A lower substitution percentage (33.3%) leads to disordered monolayers or to structures in which the alkyl chains are tilted too far ($\sim 60^\circ$) compared to the experimentally observed situation (~ 30 – 45°). Calculations on surfaces with high substitution percentages (66.7 and 100%) show that the molecules are oriented perpendicular to the Si surface. These results, thus show that the optimal substitution percentage for well-ordered monolayers on the Si (1 1 1) surface is between 50 and 66.7%.

3.2. Molecular orientation and ordering

Fourier transform infrared (FTIR) spectroscopy is the most powerful tool for studying the molecular orientation and ordering in a self-assembled monolayer [9]. FTIR is usually done in two different spectroscopy modes (i) attenuated total reflection (ATR) and (ii) reflection-absorption (RA). In the ATR mode, individual s- and p-polarized (the parallel and perpendicular components of a plane polarized light, respectively) attenuated total internal reflection spectra are recorded. The dichroic ratio

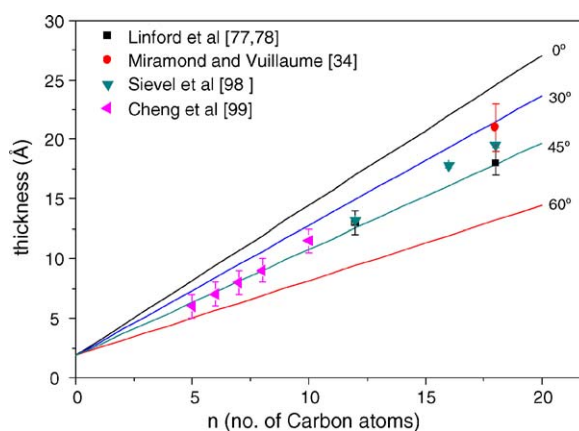


Fig. 10. Thickness of alkyl monolayers deposited on H-terminated Si measured by different groups. The full lines are the theoretical relation of thickness as a function of n , calculated using Eq. (2) at different tilt angles.

(D), defined as, $D = A^{s-pol}/A^{p-pol}$ (where A^{s-pol} and A^{p-pol} are s- and p-polarized absorbance, respectively) gives the information on the molecular orientation. Using D values of symmetric and asymmetric CH_2 stretches, one can calculate the angle between these transition dipole moments and the surface normal, i.e. α_s and α_a , respectively. These two angles, in turn, allow determination of both the chain tilt angle (Φ) and chain twist angle (γ) using the relations: $\cos^2 \Phi = 1 - \cos^2 \alpha_s - \cos^2 \alpha_a$ and $\cos \gamma = \cos \alpha_s / \sin \Phi$, respectively. It may be noted that the value of D has a steep dependence on α . For example, a change in D value from 1.04 to 1.08 would change α_a from 70 to 83°, and thus extreme care is needed in interpreting data using D values.

The peak positions of symmetric (ν_s) and asymmetric (ν_a) stretching modes of CH_2 group give the required information about the molecular order in the monolayers. For a well ordered (i.e. crystalline) monolayers the peak positions of ν_s and ν_a are at 2851 ± 1 and $2918 \pm 1 \text{ cm}^{-1}$, respectively; while for a highly disordered (i.e. liquid) monolayers these peak positions shift to 2855 ± 1 and $2924 \pm 1 \text{ cm}^{-1}$, respectively [101]. Typical IR spectra recorded for monolayers having different numbers of C atoms are presented in Fig. 11. Since ν_a —as the monolayer goes from crystalline to liquid state—shows a maximum shift of 6 cm^{-1} , we have plotted the reported ν_a in Fig. 12 for various monolayers reported by different researchers [37,77,78,101]. It is evident that for $n > 10$ the monolayers are in crystalline state; though for $n < 10$ the disorder in monolayer increases.

The information about the structure of SAMs can also be obtained by a variety of techniques, such as, X-ray [102], electron [103] and neutron [104] diffraction, high-resolution electron loss spectroscopy [105], Raman spectroscopy [106], near-edge X-ray absorption fine structure spectroscopy (NEXRAF) [107], etc.

3.3. Uniformity and coverage

The quality and uniformity of a monolayer at various lengths (from macro to nano) can be assessed by wetting measurements and/or by directly imaging the surface topography by atomic

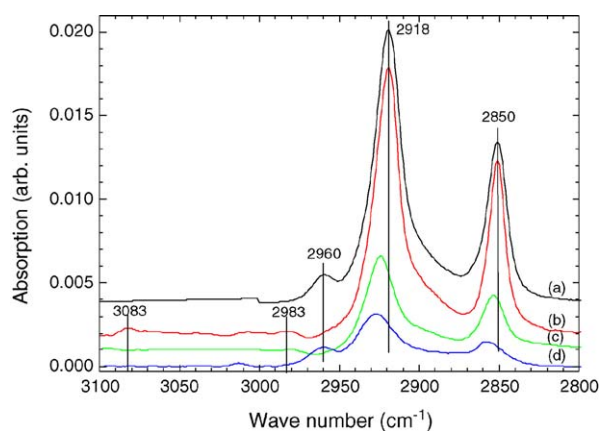


Fig. 11. IR spectra for monolayers having different numbers of C atoms: (a) 18, (b) 16, (c) 14 and (d) 8. Note a systematic shift of the ν_a (CH_2) peak, which is expected to be at 2918 cm^{-1} for a crystalline monolayer.

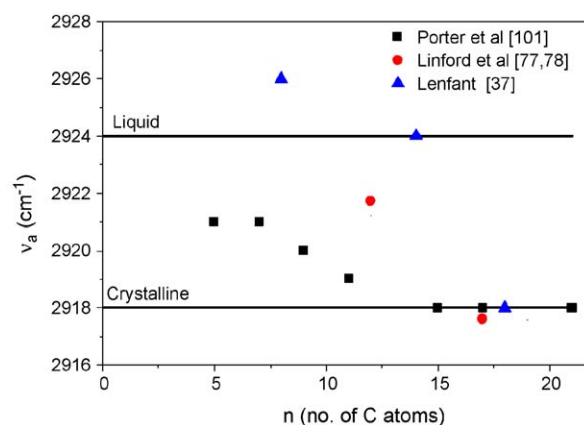


Fig. 12. Reported value of asymmetric (ν_a) stretching modes of CH_2 group for different monolayers. The values at 2918 and 2924 cm^{-1} correspond to crystalline and liquid phase of the monolayer.

force microscope, scanning electron microscopy and tunneling electron microscopy.

3.3.1. Wetting measurements

The wetting measurement is simple and effective technique because the “shape” of a liquid drop on a uniform surface depends on the free energies of the liquid and surface [9]. A drop of liquid (de-ionized water or hexadecane, for instance) is expanded on the surface using a syringe. The “advancing” and “receding” contact angles are measured. Strictly speaking the contact angle is determined by its properties of surface group, and not by the alkyl chain. However, alkyl chain indirectly affects the surface properties through ordering, packing and tilt. A summary of reported advancing water contact angle measured on monolayers with different functional head groups is presented in Table 1. It is seen that for same surface group but having different number of C atoms (n) in the chain, the contact angle is significantly lower for $n < 10$, which indicates poor ordering of

Table 1
Water contact angle measured on different functional surface group of SAMs

Head group	Contact angle (°)	Ref.
$\text{CH}_3-(\text{CH}_2)_n$ ($n > 10$)	110–117	[108,109]
$\text{CH}_3-(\text{CH}_2)_n$ ($n < 10$)	97–108	[37,110]
$\text{CH}_2=\text{CH}-(\text{CH}_2)_n$ ($20 > n > 10$)	95–105	[37]
–thiophene; –phenyl	90–92	[111,112]
–pyridyl	43	[113]
– CO_2CH_3 ; – $\text{CO}_2\text{CH}_2\text{CH}_3$; – CO_2 -benzyle; – CO_2 -thiophene; – CO_2 -anthracene; – CO_2 -pyrene; – CO_2 -EDTM	73–75	[37]
–X (Cl, Br, I)	80–89	[114–116]
–SH; –S; –S–S	65–71	[114,115]
– SO_2	50	[114]
– SO_3H	30	[114]
–SCN	73–75	[114,116]
–OH; – $\text{B}(\text{OH})_2$; – CONH_2 ; – CO_2H	<15	[117]
– NH_2	36	[114,118]
– NH_3^+	42	[114]
–CN	68–74	[114,118]
– N_3	75–79	[119]
–C60	65–76	[120,121]

monolayer. Also for $n > 20$, the contact angle decreases indicating the disorder arising probably due to the mingling of longer chains.

Zisman showed that wettability data can be used to determine the critical surface tension (γ_c) of the monolayer surface [122], which is defined as the surface tension of the test liquid that completely wets the surface, i.e. contact angle (Θ) = 0° , and is found by plotting $\cos \Theta$ versus γ_l (where γ_l is the surface tension of a series of test liquids), and γ_l value at $\cos \Theta = 1$ is equal to γ_c . For various surface head groups the γ_c could vary between 6 and 43 N/m at 20°C [9].

3.3.2. Atomic force microscopy

The surface coverage of a monolayer is usually examined by measuring the surface morphology using the atomic force microscopy (AFM). The high-resolution AFM images on a scan area of $10\text{ nm} \times 10\text{ nm}$ for the crystalline octadecyltrichlorosilane monolayer, studied by Kojio et al., exhibited a periodic arrangement of the molecules with a hexagonal array [123]. The AFM is a powerful tool for understanding the growth kinetics of SAMs [40,124–126]. In Fig. 13, we show AFM images of partial C18 monolayers, which were deposited by immersing the Si substrate in the octadecyltrichlorosilane solution for varying amounts of time [40]. Initially isolated closed packed C18 islands are formed at the surface of the substrate, and these

islands then serve as centers for aggregation for molecules diffusing on the surface as well as for adsorbing from solution (as schematically shown in the inset of Fig. 14). At low surface coverage the fractal dimension of the islands increases with surface coverage, while the height remains at $\sim 25\text{ \AA}$ indicating that C18 molecules are tilted at $\sim 30^\circ$. At higher surface coverage, the islands—height remaining at $\sim 25\text{ \AA}$ —grow by branching and eventually coalesce. With passage of time, the inter-island regions (pores or pinholes) shrink and eventually a continuous SAM get formed. In order to study the growth kinetics of the SAM formation, the monolayer coverage (Q) as a function of time, as shown in Fig. 14, is determined by analyzing the AFM images. The two regions showing different growth kinetics can be easily identified from this figure.

- (i) A faster and linear growth for time $< 5\text{ s}$ (shown by solid straight line fit), indicating that the initial growth is primarily via diffusion limited aggregation [124,125].
- (ii) For higher times, the coverage kinetics becomes slow and can be fitted to an expression $Q = 1 - \exp(-kt)$, suggesting that growth is limited by adsorption from the solution [124].

The studies on the growth kinetics as a function of chain length have revealed that while long chains grow via island nucleation and growth; the short chain did not show the island

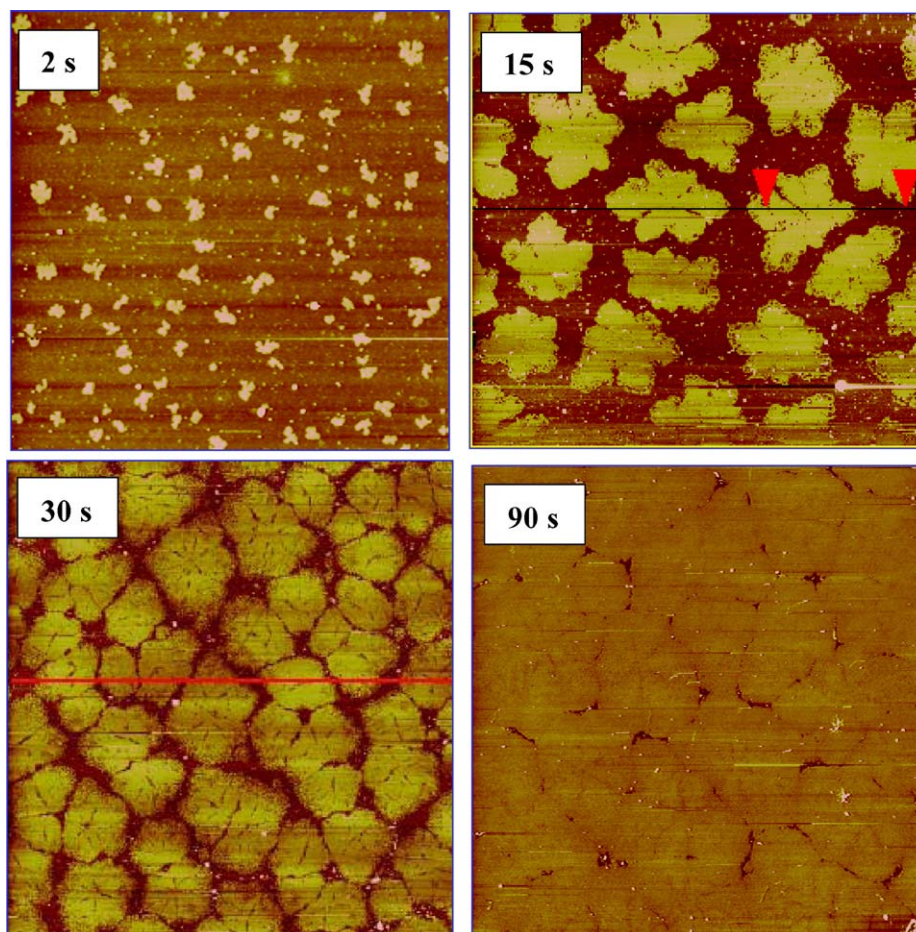


Fig. 13. $10\text{ }\mu\text{m} \times 10\text{ }\mu\text{m}$ images of partial C18 monolayer on Si immersed in octadecyltrichlorosilane (OTS) solution for varying amounts of time [40].

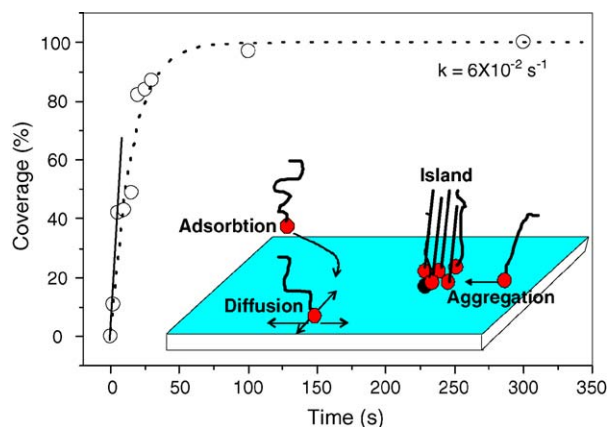


Fig. 14. Monolayer coverage as a function of time determined using analysis of AFM images presented in Fig. 13. For time < 5 s, a fast and linear growth (solid line fit) indicates that growth is due to diffusion limited aggregation. For higher time, the data is fitted (dotted line) to an equation governed by adsorption limited kinetics. Inset: Schematic showing the various processes during the monolayer growth. Once a molecule is adsorbed at the surface, it undergoes a random walk on the surface (with a certain value of 2D diffusion coefficient) until it collides with another adsorbed molecules and forms an island. Initially islands grow via diffusion-limited aggregation of adsorbed molecules followed by adsorption-limited kinetics [40].

growth behavior [126]. This has been attributed to the chain length dependent chemisorption and diffusion rates of molecules on the substrate surface, which are found to decrease with increasing chain length. However, more detailed studies are needed to confirm this mechanism. It may be noted that when the SAMs grows via island nucleation and growth mechanism, complete elimination of pinholes is not possible. These pinholes may hamper the electrical characterization of SAMs as the counterelectrode metal particulates may diffuse through them creating short-circuits. Thus, studies on the size and distribution of pinholes in SAMs are important, and must be carried out using high-resolution AFM and other techniques, such as, electrochemistry (as discussed below).

In addition, as has been discussed in the Introduction, by using a conducting AFM tip, the electrical measurements on SAMs can be carried out. Thus AFM is a unique facility in which electrical measurements as well as the morphology of the monolayer can be studied simultaneously.

3.3.3. Electrochemical

The electrochemical characterization is a sensitive tool for detection of pinholes and defects in SAMs [127,128]. In order to determine the total fraction of pinhole area, one performs cyclic voltammetry (CV) in a solution containing redox species, typically $K_3Fe(CN)_6$, and a supporting electrolyte. An ideal SAM with full coverage (Q), owing to dielectric behavior, would completely block the faradic current arising due to electrochemical oxidation of the electrode and exchange of electrons between electrode and redox couples in solution. However, presence of pinholes in the SAM allows detection of faradic current and this current is then utilized for the determination of area fractions of pinholes ($1 - Q$) [127]. It may be noted here that the faradic currents are much larger than the tunnelling currents through SAMs (see Section 5).

The redox centres, such as, ferrocene, porphyrins, tetrathiafulvalene, etc., which can be easily attached to the SAMs (the resultant is known as electroactive SAMs) serve as a sensitive and non-destructive probe for the determination of the structure of the SAM and their reactivity (surface attachment and hydrolysis reactions). A CV of an electroactive SAM usually exhibits matching anodic and cathodic current peaks, and departure from the ideal CV reveals the structural details of the SAM [128].

Using AC voltammetry one can determine the capacitance at electrode/electrolyte interface, which is then used to extract the dielectric constant of SAMs. Observed values for dielectric constant of various SAMs fall in the range 2.3–2.6. In addition, CV has been utilized for electrochemical stripping as well as deposition of SAMs [128].

3.4. Chemical composition

The chemical composition of monolayers can be determined by Auger electron spectroscopy (AES), X-ray photoelectron spectroscopy (XPS) and secondary ion mass spectrometry (SIMS) [92]. Among these XPS is a unique technique as it not only determines the chemical composition of the monolayers but also gives information on the oxidation state of its elements, and details can be obtained elsewhere [129]. The biggest advantage of XPS is that it provides the information of the surface-group of the monolayer, if spectra are recorded as a function of takeoff-angles (α : angle between the sample surface and the analyzer acceptance plane). If 95% of the signal arises from a depth into the solid of 3λ (λ is the inelastic mean free path of the emitted photoelectrons) then the depth sampled, d , is given by the equation; $d = 3\lambda \sin \alpha$. Thus, as α tends to 0° the outermost surface species account for a larger proportion of the signal detected. For example, a small molecule containing only three carbon atoms, i.e. 3-mercaptopropyltrimethoxysilane (MPTMS), $SH-(CH_2)_3-Si-(OCH_3)_3$, chemisorbed on the native silicon oxide is analyzed by XPS to find whether the $-SH$ group is at the outer surface of the monolayer or not. The XPS data of S-2s and C-1s recorded at two different take-off angles, i.e. 70° – 25° are shown in Fig. 15. The data is normalized with C-1s peak. A

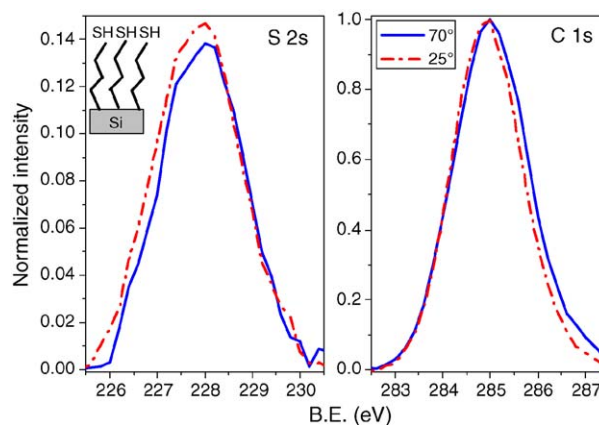


Fig. 15. Angle dependent XPS spectra of a C3 molecule having thiol group at the surface (as shown in the inset). The spectra are normalized to the intensity of C1s peak.

clear increase in sulfur content with decreasing take-off angle confirms that the $-SH$ group is at the outer surface and the silane group is attached to the native silicon oxide.

3.5. Thermal and chemical stability

In order to use SAMs in molecular electronics and/or hybrid electronics, it is essential that SAMs must remain robust under the same daunting conditions that all existing semiconductor materials already endure. These include thermal stability up to 350°C , chemical stability under different etchants, endurance etc. Therefore, the SAMs have been subjected to stability tests under a wide variety of conditions, which includes high temperatures, acids, base etc. [7,37,52]. The common method to check the stability is to measure the thickness and contact angle as a function of the treatment. Most remarkably the SAMs exhibit no signature of degradation when stored in an airtight container for 18 months [52].

Typical temperature, acid and base stability of C18 SAMs is plotted in Fig. 16. The C18 SAM is stable up to a temperature of $\sim 350^{\circ}\text{C}$, and at higher temperatures the SAMs evaporate from the substrate surface. The thermal stability was found to be independent of the chain length [7,37]. The high-energy electron loss energy spectroscopy (HREEL) measurements reveal that at temperature higher than 350°C the SAM begin to decompose primarily through the cleavage of C–C bonds [110]. The siloxane head group (Si–O) is strongly bonded to the substrate surface and begins to decompose only after 725°C . As will be discussed

in Section 6.3, the molecular memories based on redox-active molecules grafted by self assembly on Si have been found stable up to 400°C .

The SAMs are remarkably stable when washed using 1% detergent solution, hot tap water or organic solvents [7]. As shown in Fig. 16(b), the C18 SAMs are stable in contact with aqueous acid at room temperature for long periods (up to a couple of days). However, SAMs get immediately deteriorated on exposing to aqueous base, and a complete removal of monolayer was observed within 60 min. The destruction of monolayer in the base is due to the hydrolysis of Si–O bonds [52].

4. Metal counterelectrodes on SAMs

As discussed in Section 2.1, Fig. 1, for the measurement of the electronic transport properties of SAMs and fabrication of molecular electronic devices using them, fabrication of metal counterelectrodes is an important step. An essential criterion for the fabrication of metal counterelectrodes is that during the process it should not damage or short-circuit the monolayer. The various types of counterelectrodes and their fabrication processes are described below.

4.1. Liquid Hg contacts

To measure the electrical properties of organic monolayers, ‘soft’ contacts, such as, electrodes in solution or the use of mercury has been employed [130,131]. Mercury, being liquid at room temperature, moulds into the surface topology of the monolayer and does not damage the monolayer. Experiments carried out using mercury-hanging drop electrodes have demonstrated the viability of organic monolayers in the electronics. While soft contacts based on liquid mercury are useful for generating experimental data, which in turn, improve our understanding of the interfaces and molecular properties, they are unsuitable for practical fabrication in the electronics industry.

4.2. Vacuum deposition

In order to have compatibility with photolithography and electron beam lithography processes to fabricate well defines structures, metal contacts are directly deposited onto the monolayer surface. The conventional deposition methods viz. thermal evaporation, electron-beam evaporation or sputtering, can be used for the deposition of metal counterelectrodes. However, these techniques—owing to the impingement of high energetic metal flux—can damage the monolayer by altering their structure significantly and/or metal atoms can diffuse through the monolayers causing short-circuits. Two methods have been used to avoid the metal diffusion (i) cooling the samples up to liquid nitrogen temperature during evaporation [132], and (ii) choosing appropriate surface group of the monolayer, which forms chemical bonds with metal. For example, the terminating $-SH$ group of monolayer forms covalent bonds with first deposited Au atoms and thus stop the diffusion of Au [33].

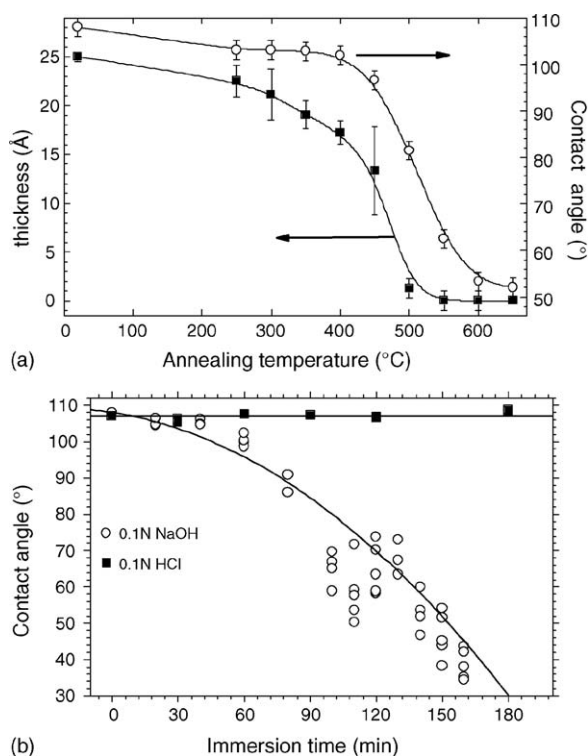


Fig. 16. (a) Thickness and water contact angle of C18 SAM measured as a function of annealing temperature. The annealing was carried out for 30 min under He ambient. (b) The water contact angle on C18 SAM as a function of immersion time in 0.1N NaOH and 0.1N HCl [37].

Another critical aspect of direct metal deposition on monolayers is the thickness of the metal layer, as the growth morphology of ultra-thin metal films, apart from other parameters, depends on the surface free energies of the metal and the monolayer. For Au thickness <10 nm, metal grows via 3D island growth and forms discontinuous film, which makes them unsuitable for electrical measurements. On the other hand, high Au thickness often leads to short-circuits in monolayers, because during thermal deposition of Au, for higher thickness the monolayer is exposed for prolonged duration of high energetic Au flux, which damages the monolayer and allows the diffusion of Au. Usually Au thickness in the range 20–80 nm thickness on as monolayers terminated with $-SH$ group has been found optimum. However, in order to obtain a comprehensive coverage of metal on the monolayer having different terminating groups, without short-circuiting, one needs to optimize the thickness of the metal.

The advantage of direct metal deposition method is that two- or three-terminal devices can be fabricated by simply depositing metal through the well defined mask structures. However, this approach produces devices with blurred edges. In order to produce devices with fine features, one can employ the photolithography for micro size features and electron beam lithography for sub-micron size features.

4.3. Soft lithography

“Soft lithography” is a new high resolution patterning technique developed by Whitesides, and comprehensive reviews on this subject are available [133,134]. This technique can be used for different purposes, e.g. patterning of SAM on different substrates, patterning of counterelectrodes on SAM, etc. Here, we are interested in patterning of metal electrodes on the SAM using soft lithography—also known as nano-transfer printing (nTP). The nTP process, as schematically shown in Fig. 17, consists of four major steps: (i) a “stamp” with desired pattern is made from an elastomeric material called polydimethylsiloxane (PDMS) and, is subjected to a surface treatment, such as, plasma etching and perfluorination (dipping stamp in 35 ml hexane, 15 ml CCl_4 and 50 μ l of $C_{10}F_{17}H_4SiCl_3$ solution) in order to have a poor adhesion of Au, (ii) deposition of Au (20–200 nm thickness) film

using thermal or e-beam evaporation; during deposition care must be exercised to avoid cracking or buckling of stamp, and in turn, of the metal film, (iii) the stamping of the monolayer (usually done at room temperature for few tens of seconds) and (iv) the removal of stamp leads to the transfer of Au patterns on SAM; during the intimate contact between stamp and SAM, a high density of bonding sites present at the surface of monolayer (e.g. $-SH$ group) allows an efficient transfer of Au, as Au and S are known to form covalent bonds. By using nTP process, Au patterns, free from defects and cracks, over large areas have been demonstrated.

5. Electronic conduction in SAMs

The SAMs of aliphatic chains are expected to be dielectric in nature owing to a very high gap between highest occupied molecular orbital (HOMO) and lowest unoccupied molecular orbital (LUMO). The theoretical calculations show that the HOMO–LUMO gap in aliphatic chains could be as large as 9 eV [135]. In fact, our studies on SAMs of *n*-alkyltrichlorosilanes ($n > 8$ carbon atoms) indicated that the leakage current through them is remarkably low ($<10^{-8}$ A/cm²), and thus could be used as dielectric in organic thin film transistors (OTFT) [42–45]. Later on, SAM dielectric films were indeed successfully employed for the fabrication of OTFT's by us [36,39] as well as by other groups [136]. In this Section, first we present a brief summary of various theoretical models that can explain the electronic conduction in a dielectric SAM, and then analyze some of the experimental results using these models on alkyl chains of different lengths.

5.1. Theoretical models

A SAM of aliphatic chains sandwiched between two metal electrodes (e.g. highly degenerated p^+ or n^+ Si and metal counterelectrode) can be represented by an equivalent energy band diagram of a metal(1)–insulator–metal(2) (M_1 – I – M_2) structure. In an M – I – M structure, the electronic conduction can take place by four different mechanisms, namely, tunneling, thermionic emission, Poole–Frankel emission and hopping conduction. Here, we briefly discuss the basics of these conduction mechanisms. The schematic energy band diagrams, along with temperature and voltage dependences of the current densities, of various conduction mechanisms have been summarized in Table 2.

5.1.1. Tunneling

A simple model of the tunneling in a M – I – M structure is given by a current of electrons, which encounter a finite potential barrier (ϕ) at the metal–insulator interface. Even though the energy of the electrons is lower than the ϕ , their wavefunctions do not vanish at the interface, but fall off exponentially into the barrier [137]. This implies that there is a finite probability that electrons from either of the metal electrodes can travel a short distance into the insulator despite the lack of allowed energy levels there. The overlapping of the wavefunctions gives rise to a non-resonant tunneling current density. Simmons has shown that the theoretical relationship between direct tunneling current

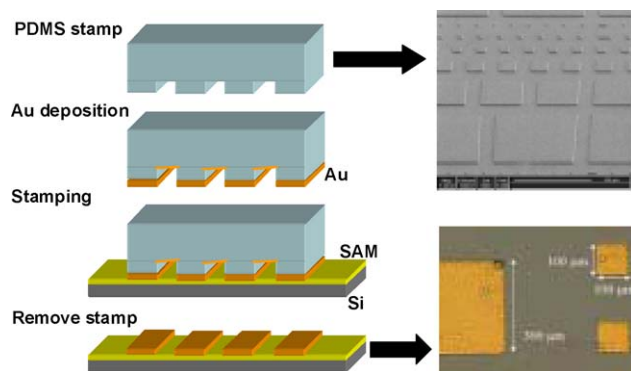
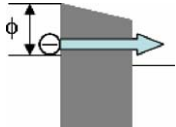
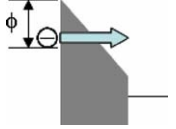
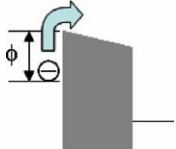
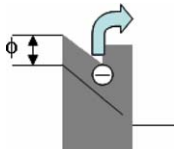
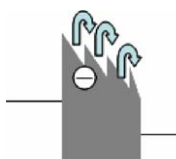


Fig. 17. Left: Schematic showing the different steps in the nTP process for Au pattern transfer on SAM. Right: Photographs of the first (PDMS stamp) and the last steps (Au transfer on a SH terminated SAM).

Table 2

Various possible electronic conduction mechanisms in a MIM structure, their schematic energy band diagrams, and voltage and temperature dependences of resulting J

Conduction mechanism	Energy band diagram	Voltage dependence	Temperature dependence
(a) Tunneling			
Direct		(1) for $eV \ll \phi$ or $V \approx 0$, $J \propto V$ (2) for $eV < \phi/2$, $J \propto V + V^3$	None
Fowler–Nordheim		(3) for $eV > \phi/2$, $\ln(J/V^2) \propto 1/V$	None
(b) Thermionic emission			
		$\ln(J) \propto V^{1/2}$	$\ln(J/T^2) \propto 1/T$
(c) Poole–Frankel emission			
		$\ln(J/V) \propto V^{1/2}$	$\ln(J) \propto 1/T$
(d) Hopping conduction			
		$J \propto V$	$\ln(J/V) \propto 1/T$

density (J_{DT}) and V for a trapezoidal barrier is given by [33,138]

$$J_{DT} = \frac{\alpha}{d^2} \left[\phi e^{-Ad\sqrt{\phi}} - (\phi + eV)e^{-Ad\sqrt{\phi+eV}} \right] \quad (3)$$

where $\alpha = e/4\pi^2\beta'^2\hbar$ and $A = 2\beta'\sqrt{2m^*/\hbar^2}$ (e is the electron charge, m^* is the effective mass of electron in the insulator, β' is a constant and has value ~ 1 , \hbar is the reduced Planck's constant), ϕ is average barrier height, d is the barrier width and V voltage between the electrodes.

It has been shown that at very small voltages, i.e. for $eV \ll \phi$, or in the vicinity of $V \approx 0$, the Eq. (3), reduces to [138]

$$J_{DT} = \frac{\gamma\sqrt{\phi}}{d} e^{-AD\sqrt{\phi}} V \quad (4)$$

where

$$\gamma = \frac{e\sqrt{2m^*}}{4\beta'^2\pi^2\hbar^2}.$$

Since $eV \ll \phi$, it can be considered that ϕ does not depend on V . Therefore, in this case the J is proportional to V .

For *intermediate voltages*, i.e. $eV < \phi/2$, the Eq. (3) is expressed as [138]

$$J_{DT} = \frac{\gamma\sqrt{\phi}}{d} e^{-Ad\sqrt{\phi}} (V + \sigma V^3) \quad (5)$$

where

$$\sigma = \frac{(Ae)^2}{96\phi d^2} - \frac{Ae^2}{32d\phi^{3/2}}.$$

For *high voltage range*, i.e. $eV > \phi$, the potential barrier takes a triangular shape, as shown in Table 2, and Eq. (3) reduces to the usual Fowler–Nordheim form [138], i.e.

$$J_{FN} = BE^2 \exp\left(-\frac{C}{E}\right) \quad (6)$$

where $E = V/d$ is the field across the monolayer, $B = e^3/16\pi^2\hbar m^*\phi$ and $C = (4\sqrt{2m^*}/3e\hbar)\phi^{3/2}$. If the current transport across a dielectric layer is dominated by FN tunneling then a plot of $\ln(J_{FN}/E^2)$ versus $1/E$ —known as FN plot—should have a linear behavior, and the intercept with y-axis and the slope of the plot would yield the values of B and C , respectively. Once the values of B and C are known, the values of m^* and ϕ can be calculated, without assuming the value of any of the two parameters.

In addition to the above-mentioned non-resonant tunneling mechanisms, i.e. direct and Fowler–Nordheim, a resonant tunneling may occur through the molecular orbitals of SAMs, if the HOMO–LUMO gap is relatively small, e.g. for π -conjugated molecules.

5.1.2. Thermionic emission

Within a metal, the energy distribution of electrons is given by the Fermi–Dirac distribution function. This implies that at elevated temperatures, an increasing fraction of the electrons in the metal will have sufficient energy to surpass the energy barrier offered by the insulator. As a result, as illustrated in Table 2, these energetic electrons can travel across the insulator, and this process is known as “thermionic emission”. The resulting current density is expressed by [1,139]

$$J_{\text{TE}} T^2 e^{-(\phi - e\sqrt{eV/4\pi\epsilon d})/kT} \quad (7)$$

where k is the Boltzmann constant.

5.1.3. Poole–Frenkel emission

If the insulating layer contains structural imperfections, such as, defects or impurity atoms, then these defects can act as electron traps. Field-enhanced thermal excitations of the trapped electrons then contribute to the current density, which is expressed by [139]

$$J_{\text{PF}} V e^{-(\phi_B - e\sqrt{eV/4\pi\epsilon d})/kT} \quad (8)$$

where ϕ_B is the trap barrier height, as illustrated in Table 2. This process is called Poole–Frenkel (PF) emission, and is a thermally activated process.

5.1.4. Hopping conduction

If the insulator has large defects/impurities, then the electronic conduction takes place via hopping mechanism. The current density in this case is given by [139]

$$J V e^{-\Delta E/kT} \quad (9)$$

where ΔE is the electron activation energy.

5.2. Tunneling in short alkyl chains

As seen from Table 2, the tunneling mechanisms are temperature independent but depend on the applied bias range, that is, direct tunneling takes place at lower bias and a crossover to Fowler–Nordheim tunneling takes place at higher bias. On the other hand, thermionic emission, Poole–Frankel emission and hopping conduction mechanisms depend on temperature. Thus, in order to identify the conduction mechanism responsible in a particular SAM, it is essential that J – V data should be taken over a large voltage range as well as their temperature dependence measured. The resultant temperature dependent J – V data then can be analyzed using above discussed theoretical models.

We have recently initiated investigations on the tunneling mechanism in a SAM of short alkyl chains [33]. We have chosen p^+ -Si(SiO_x)/3-mercaptopropyltrimethoxysilane (MPTMS;

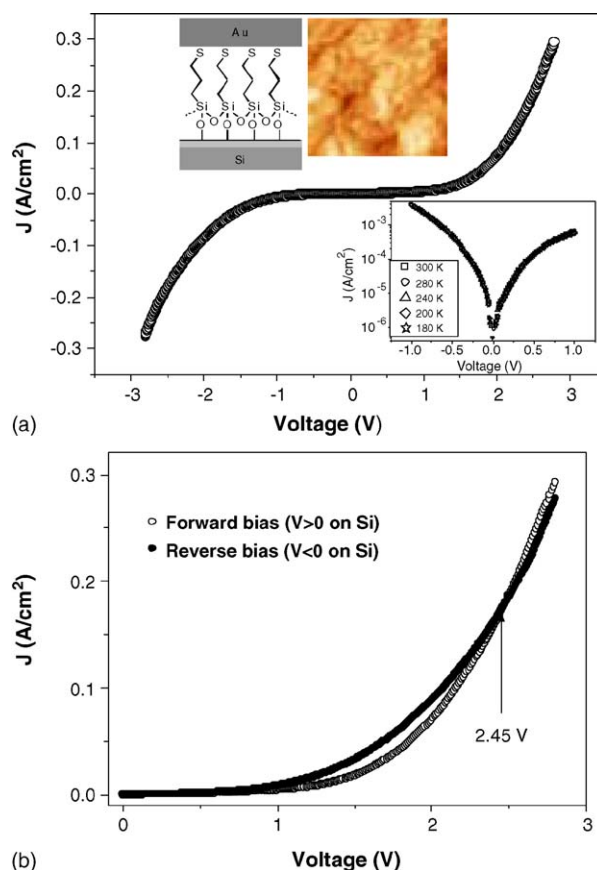


Fig. 18. (a) Typical current density–voltage curve recorded for the MPTMS SAM at room temperature. Upper-left inset: schematic of the Si/SiO₂–MPTMS–Au structure and, 200 nm × 200 nm AFM image of top gold electrode, indicating comprehensive coverage of the monolayer. Bottom-right inset: J – V curves in the semi-log scale in ± 1 V range at different temperatures. (Note that all the curves are identical at different temperatures, and were also independent of heating or cooling schedules.). (b) The plots of absolute values of J and V in reverse as well as forward bias. Note a crossover at 2.45 eV.

SH–(CH₂)₃–Si–(OCH₃)₃/Au structure for the following reasons: (i) the SAM contains the aliphatic chain of only three carbons and has a very short length (0.8 nm), and thus, as revealed from Eq. (4), a high direct tunneling current is expected, and (ii) the outer surface of SAM is terminated with thiol (–SH) group, which prevents diffusion of counterelectrode Au owing to strong chemical bonding between S and Au, as discussed in Section 4.

A typical J – V curve for the MPTMS monolayer measured at 300 K is given in Fig. 18(a). Two major inferences can be drawn from this figure: (i) the J – V curves are asymmetric, which becomes clear when we plot both forward ($V > 0$ on Si) as well as reverse bias ($V < 0$ on Si) data in the same quadrant (Fig. 18(b)) and (ii) the J – V data are independent of temperature, which indicate as discussed above, that tunneling is the mechanism of the conduction in this SAM.

From Fig. 18(b) and from J – V plots as a function of temperature, it is evident that at low bias the reverse current is higher than the forward one. However, at bias greater than 2.45 eV, the direction of rectification is reversed, i.e. the forward current is higher than the reverse current. This result is not unexpected,

and such an effect has been predicted theoretically by Simmons, way back in 1963 [138], for a thin insulating film sandwiched between two metal electrodes of different work functions, i.e. metal(1)–insulator–metal(2) (M_1 –I– M_2) junction. In the present case, the work functions of two electrodes (i.e. p^+ -Si and Au) are, respectively, $\psi_1 = 4.9$ and $\psi_2 = 5.3$ eV [140]. Thus, a qualitative comparison with Simmons theory indicates that the MPTMS monolayer has a very good insulating behavior, and tunneling is the conduction mechanism. Thus, the J – V data of Fig. 18 can be quantitatively analyzed using Simmons' Eqs. (3)–(6). For this purpose, depending upon the bias range, the J – V data has been replotted in three different zones, as shown in Fig. 19.

At very low bias, i.e. ± 0.15 V, as shown in Fig. 19(a), the data fits well to a linear equation, which is in accordance with Eq. (4). The slope of linear fit yields a resistance of $4850 \pm 30 \Omega \text{cm}^2$ for the MPTMS monolayer. The data in the intermediate voltage range 0–1.3 V, as shown in Fig. 19(b), fit well to Eq. (5) using parameters $m^* = 0.16m_e$ (m_e = mass of the electron), $d = 2$ nm (length of MPTMS molecule + thickness of native SiO_2) but with different ϕ values in the reverse and forward bias. The fitting of reverse bias data yielded $\phi_1 = 2.14 \pm 0.01$ eV, which corresponds to the electron energy barrier height at MPTMS/Si interface; while an electron energy barrier of $\phi_2 = 2.56 \pm 0.01$ eV is obtained at MPTMS/Au interface by fitting the forward bias data. The difference in barrier heights (i.e. $\Delta\phi = 0.42$ eV) is

nearly equal to the difference in the work functions of the two electrodes, which is in accordance with Simmons theory. The value of $m^* = 0.16m_e$ obtained from the fitting is same as experimentally reported by others [20] and close to $m^* = 0.28m_e$ calculated theoretically for n -alkanes [141]. With these values of m^* and ϕ , we deduce a tunneling decay factor ($\beta = A\phi^{0.5}$ in Eq. (4)) of $\sim 0.65 \text{ \AA}^{-1}$, which is within the range of 0.5 – 0.75 \AA^{-1} determined experimentally by several authors [24].

In the FN region, as shown in Fig. 19(c), the data is plotted as $\ln(J/E^2) - 1/E$ using $d = 0.8$ nm. A good linear fit of the data (for $V > 1.3$ V) confirms that at higher voltages the mechanism of conduction in Si/SiO₂–MPTMS–Au structure is due to the Fowler–Nordheim tunneling. Using the values of constants A and B obtained from FN plots, the determined values of m^* and ϕ for 17 samples are shown by the pie charts in Fig. 19(c). The value of m^* is found to be in the range $0.10m_e$ – $0.22m_e$, with the majority of the values lying in the range $0.15m_e$ – $0.18m_e$, and is somewhat closer to the theoretically estimated value of $0.28m_e$ [141]. Similarly, values of ϕ were found to vary between 1.22 and 2.31 eV, and the majority of values lying in the 1.3–1.5 eV range, which is about ~ 1 eV less than ϕ_{SAM} . As shown in the inset of Fig. 17(c), the image force potential lowers the barrier height, which is given by $\phi_{\text{IF}} = (\phi_{\text{SAM}} - \phi) = 2\sqrt{e^2 E / \epsilon_{\text{SAM}}}$, where ϵ_{SAM} is the dielectric constant of the monolayer [142]. For $E = 4 \times 10^7$ V/cm and using $\epsilon_{\text{SAM}} \sim 2.5$ for the monolayer

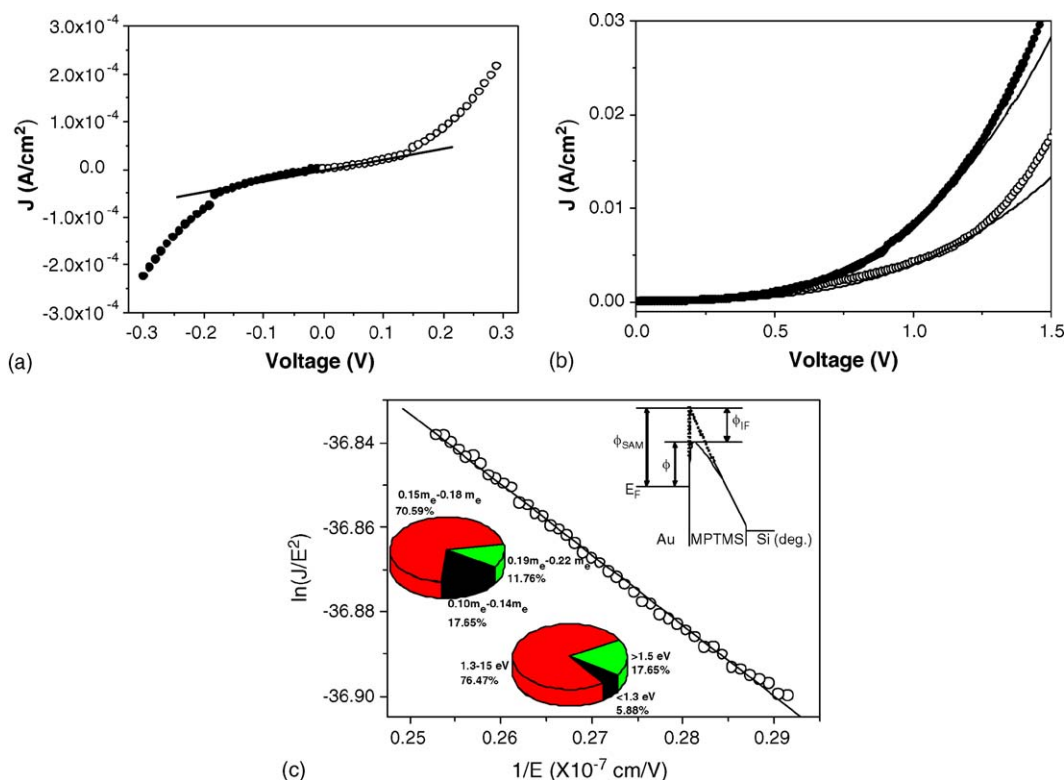


Fig. 19. Data of Fig. 1(a) replotted in three voltage regions (filled circles represent to reverse bias data and open circles to forward bias). (a) Low voltage range, i.e. ± 0.3 V. The linear fit of data (shown by full line) in ± 0.15 V bias range is in accordance with Eq. (4). (b) Intermediate voltage range. The full curves are fit of data using Eq. (5) with parameters $m^* = 0.16m_e$ (m_e = mass of the electron), $d = 2$ nm (length of MPTMS molecule + thickness of native SiO_2) but with different ϕ values in the reverse ($\phi_1 = 2.14 \pm 0.01$ eV) and forward ($\phi_2 = 2.56 \pm 0.01$ eV) bias. (c) High voltage range data (i.e. > 1.3 V) is plotted as $\ln(J/E^2)$ as a function of $1/E$. A linear fit of the data indicate that current transport is dominated by Fowler–Nordheim tunneling. Top right inset: an energy band diagram showing the lowering of triangular energy barrier (dotted) by image force potential (full curve). Bottom left inset: pie charts showing the distributions of effective mass (m^*) and energy barrier height (ϕ) determined from the FN plots of 17 samples.

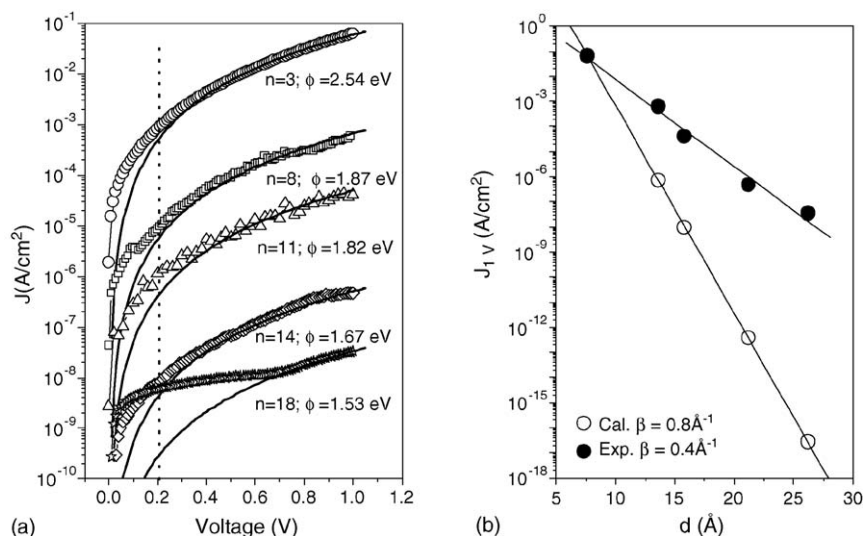


Fig. 20. (a) The J - V data for CH₃-terminated n -alkanes ($n=8, 11, 14$ and 18 carbon atoms) SAMs. For comparison the data of SH-terminated 3-alkane SAM is also plotted. The full curves are data fit using Simmons Eq. (5). (b) The plot of J (at 1 V) as a function of molecule length. Filled circles correspond to experimentally measured; while open circles are the calculated values using Eq. (5) and assuming $\phi = 2.54$ eV, and $m^* = 0.16m_e$.

[9,44], the calculated value of ϕ_{IF} is ~ 1 eV, which is nearly the same as the difference between ϕ_{SAM} and ϕ , confirming that the low ϕ values obtained at high fields are due to the image force potential.

5.3. Length dependent electrical properties

The J - V data for CH₃-terminated n -alkanes ($n=8, 11, 14$ and 18 carbon atoms) SAMs with Al as counterelectrode are presented in Fig. 20(a). The fit of these data in the intermediate bias range, i.e. between 0.2 and 1 V, using Simmons Eq. (5) indicates that as the chain length increases, the fittings turns poorer. In addition, the determined ϕ value reduces with increasing chain length, and becomes as low as 1.5 eV for $n=18$ SAM. On the other hand, the internal photoemission data, as shown in Fig. 21, measures a ϕ value in the range 4.1 – 4.3 eV, which is much higher than that determined from the transport measurements. It may be noted that low ϕ values (2 – 2.5 eV) for long chain SAMs have been measured when counterelectrode forms a chemical bond

with the surface group of the monolayer [19,24,129,143]. It is believed that the chemical bonds with electrodes would decrease the HOMO–LUMO gap of the alkyl chains and, which in turn, lower the barrier height. Apart from this a wide variation in ϕ values obtained from J - V data could be either due to improper counterelectrodes, which implies that the metal electrode has diffused into the monolayer, and/or deliberate fitting of data using Simmons model, which essentially may not be arising from the tunneling conduction mechanism alone.

Supposing tunneling is the lone conduction mechanism in n -alkane SAMs, then theoretical J (at 1 V), calculated using Eq. (5) and assuming $m^* = 0.16m_e$ and $\phi = 2.5$ eV, as a function of chain length can be plotted as shown in Fig. 20(b). A comparison with experimental data indicates that the experimentally observed J values are much higher than that expected from the tunneling conduction mechanism. There are two possibilities for enhanced J values: (i) the counterelectrode metal may diffuse through the monolayer, as the terminating CH₃ group does not form chemical bonds with Al, leading to additional filamentary conduction channels, and (ii) the electronic conduction mechanism may be changing from tunneling to some other (see Table 2) mechanism(s) with increasing chain length. The best way to resolve this issue is to conduct temperature dependent J - V studies on SH-terminated n -alkanes SAMs with Au as counterelectrode, and analyze the data using various models presented in Table 2.

Similarly, the reported tunneling decay parameter (β), usually obtained from the slope of J - d plots, has a wide range from 0.4 to $>1 \text{ Å}^{-1}$ (this range of β includes monolayers of alkanethiol on gold as well as alkanes on Si) [24]. As shown in Fig. 20(b), the value of β obtained from theoretical J - d plot is 0.8 Å^{-1} while that obtained from the experimental plot is $\sim 0.4 \text{ Å}^{-1}$. A low β value is an indication of high tunneling efficiency. However, as discussed above, one can obtain higher J values due to altogether different reasons viz. additional filamentary conduction channels and conduction mechanism(s) different than tunneling, and thus a low β value. A more consistent β value is

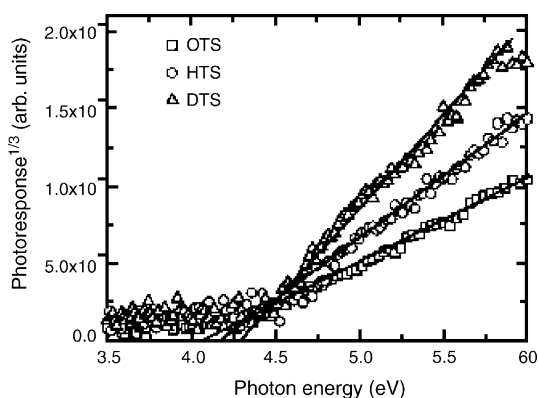


Fig. 21. Cubic root of the photoresponse (photocurrent divided by the photon flux) vs. the photon energy for three OTS ($n=18$), HTS ($n=16$), and DTS ($n=12$) monolayers. The obtained ϕ values are 4.1 , 4.2 and 4.3 eV, respectively.

expected, if one conducts the experiments on high quality SH-terminated *n*-alkanes ($n > 8$) SAMs. Unfortunately, deposition of SH-terminated *n*-alkanes ($n > 8$) SAMs using multi-step process revealed very low yield of the –SH group at the surface, and thus new chemical methods need to be explored to achieve higher yields.

5.4. Dielectric breakdown of SAMs

It is clear from the previous Section that the leakage current through the alkane SAMs is quite low. However, for using them as a dielectric in electronic devices, low leakage current is not the only concern. Under high field stress, insulating films will eventually reach breakdown [139], which causes an irreversible damage leading to increased leakage current and eventually fatal device failure. The physical meaning of breakdown is the destruction of the atomic structure by breaking inter-atomic bonds. Various imperfections can cause an insulating material to break down at a lower voltage than anticipated. Such events are usually related to charge buildup for some reason, which locally increases the electric field. Thus, an insulator material is also characterized by a breakdown electric field.

The simplest way of investigating the electric breakdown in an insulator is to record J – V data to very high voltages till one observes a breakdown. Fig. 21 presents a typical J – V curve for a MPTMS SAM at voltages > 3.2 V. It is seen that for voltages > 3.6 V, named as pre-breakdown region, the FN current jumps to either a high conduction state (i.e. high J values) or a low conduction state (i.e. low J values) or both (as in the present case). The conduction state of current jump and its occupying voltage range are random in nature. The hard breakdown of the monolayer is observed to take place between 3.6 and 4.1 V. Once the hard electric breakdown of monolayer has taken place, the next voltage ramp always leads to a higher J and its linear relationship with V , suggesting creation of stress-field induced permanent defects in the monolayer during the breakdown process.

In order to understand the breakdown mechanism, theoretical J – V curves in the pre-breakdown region (shown by full lines in Fig. 22) are calculated using the FN Eq. (6), with known m^*

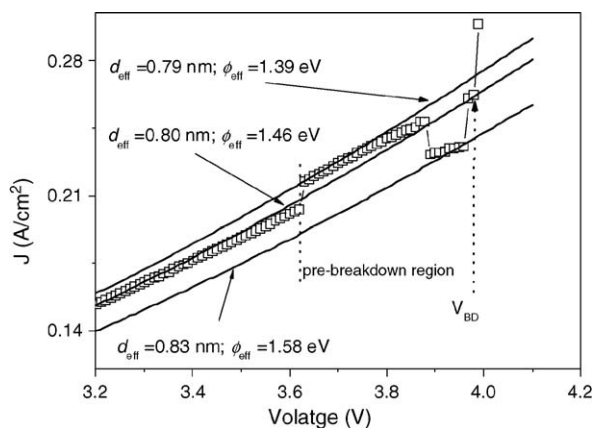


Fig. 22. J – V plot in the pre-breakdown region. The full lines are the theoretical FN (Eq. (6)) curves calculated using known m^* and ϕ for different effective thickness (d_{eff}), as discussed in the text.

and ϕ values but different effective electrical thickness (d_{eff}) corresponding to different FN current jump states. Since the thickness of SAM is fixed, a change in d_{eff} implies that the electrical properties of monolayer are affected owing to the creation of defects by high FN tunnel currents, and this should also be reflected as a change in ϕ [144]. Once d_{eff} for a particular current jump state is known, then ϕ_{eff} is back calculated using FN plot. It is evident that lowering of d_{eff} lowers the ϕ_{eff} , and vice versa. A decrease in d_{eff} or ϕ_{eff} implies high tunnel currents and the additional current can be explained using the defect-assisted conduction/tunneling. On the other hand, trapping of electrons at the generated defects will increase the ϕ_{eff} , or in other words, would increase the value of d_{eff} and hence, lower the current through the monolayer. Once the hard breakdown occurs at around 4 V, the monolayers become conductive owing to the creation of permanent electric defects. Considering the fact that the native oxide does not remain a dielectric at such high voltages, the calculated breakdown field, $E_{\text{BD}} = V_{\text{BD}}/d_{\text{SAM}}$, for the MPTMS monolayer comes out to be ~ 50 MV/cm. This value is much larger than the 12–20 MV/cm reported for longer alkane chains (no. of carbon atoms > 10) using different systems viz. octadecyltrichlorosilane on SiO_x/Si [47], alkanethiol on gold [17] and alkanes on H-terminated Si [145], suggests that the shorter chains have higher breakdown fields. This is believed to be due to a reduction in impact ionization at reduced thickness, and needs further investigations. On the other hand, supposing that the native oxide is a perfect dielectric and we take its thickness into consideration, then the breakdown field, $E_{\text{BD}} = V_{\text{BD}}/d_{\text{ox}} + d_{\text{SAM}}(\epsilon_{\text{ox}}/\epsilon_{\text{SAM}})$, is ~ 16 MV/cm, which is still much larger than the breakdown field of equivalent thickness (i.e. ~ 2 nm) of SiO_2 [146], suggesting suitability of these monolayers for hybrid electronics.

6. Molecular devices

As has been demonstrated in the previous Section, the alkane chains (σ molecules) show very good dielectric properties with very high electric breakdown fields owing to a large HOMO–LUMO gap. On the other hand, the π -conjugated molecules owing to the delocalized electrons exhibit high electrical conductivity. Since the organic chemistry allows to couple σ - and π -molecules and these organic molecules can be grafted on Si surface by self-assembly, by choosing an appropriate architecture of σ - and π -molecules various active electronic components can be fabricated. In this Section, we discuss the concepts and fabrication of some such molecular devices, and their characteristics.

6.1. Molecular diodes

6.1.1. Basic concepts

The first theoretical idea on molecular rectifying diode was proposed by Aviram and Ratner, which is based on donor (D) and acceptor (A) moieties linked by a short bridge (b) [3]. This A–b–D molecule, having σ and π bridge, is ω -substituted by an alkyl chain to allow a mono layer formation by the Langmuir–Blodgett (LB) method, and this LB monolayer is

then sandwiched in a metal/monolayer/metal junction. Up to now, the most interesting results to date were obtained with the hexadecylquinolinium tricyanoquinodimethanide molecule ($C_{16}H_{33}-Q-3CNQ$) [147]. However, the maximum chemical synthesis yield of this molecule is only $\sim 59\%$ [148]. It has been demonstrated that the donor and acceptor groups in this molecule are not sufficiently isolated by the π -bridge, and the molecular orbitals are too delocalized over the entire $Q-3CNQ$ unit to allow a correct implementation of the AR paradigm [35]. The rectification effect was attributed to the geometrical asymmetry induced by the long alkyl chain which places the $Q-3CNQ$ unit close to one of the electrodes (inducing an asymmetric electrostatic profile across the molecule). Subsequently, theoretical studies of this asymmetry effect have been conducted more extensively [149]. These results thus indicate that rectifier effect should be expected from the molecules having only one donor group and an alkyl spacer chain, and the concept of such a molecular rectifier is shown schematically in Fig. 23.

6.1.2. Chemical synthesis

The synthesis of diodes based on σ - π molecules, as shown in Fig. 24, is carried out by three sequential self-assembly processes (i) silanization, (ii) oxidation and (iii) esterification [37]. In the first step, i.e. silanization, the vinyl-terminated alkyl chains with several lengths namely, heptadec-16-en-1-trichlorosilane (HETS, $SiCl_3-(CH_2)_{15}-CH=CH_2$), tetradec-13-en-1-trichlorosilane (TETS, $SiCl_3-(CH_2)_{12}-CH=CH_2$) and oct-7-en-1-trichlorosilane (OETS, $SiCl_3-(CH_2)_6-CH=CH_2$) are grafted on degenerated Si substrates by self assembly process, as has been discussed in Section 2. In the second step, the vinyl end-groups are substituted by $-COOH$ group

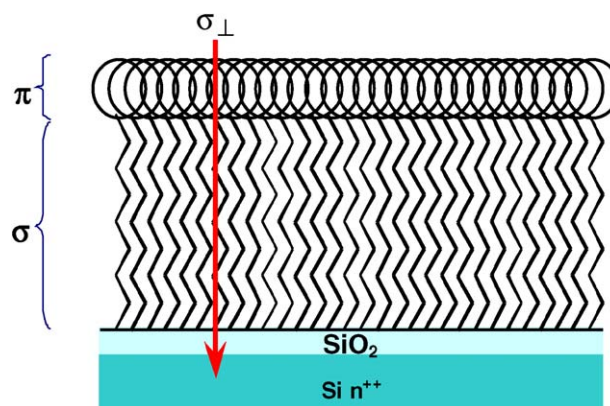


Fig. 23. A schematic showing the concept of a σ - π molecular rectifier on Si. An asymmetric electrostatic profile across the molecule causes rectification.

using oxidation, which is carried out in aqueous solution of $KMnO_4/NaIO_4/K_2CO_3$. The yield of this oxidation has been estimated between 70 and 90%. In the final step, the conjugated moieties are grafted onto the previously formed SAMs using esterification reactions between the $COOH$ end-groups and different alcohols, which are shown in Fig. 24. The esterification is carried out in the presence of a water trap (dicyclohexylcarbodiimide, DCCI) at room temperature for prolonged durations (120 h) to enhance the reaction yield. After each step, the monolayers are characterized by contact angle, ellipsometry and FTIR (as discussed in Section 3) to establish the occurrence of correct chemistry at the surface of the monolayer. Unfortunately, the chemical yield of this process is around 30–40%, and new chemical routes need to be explored to enhance the yield.

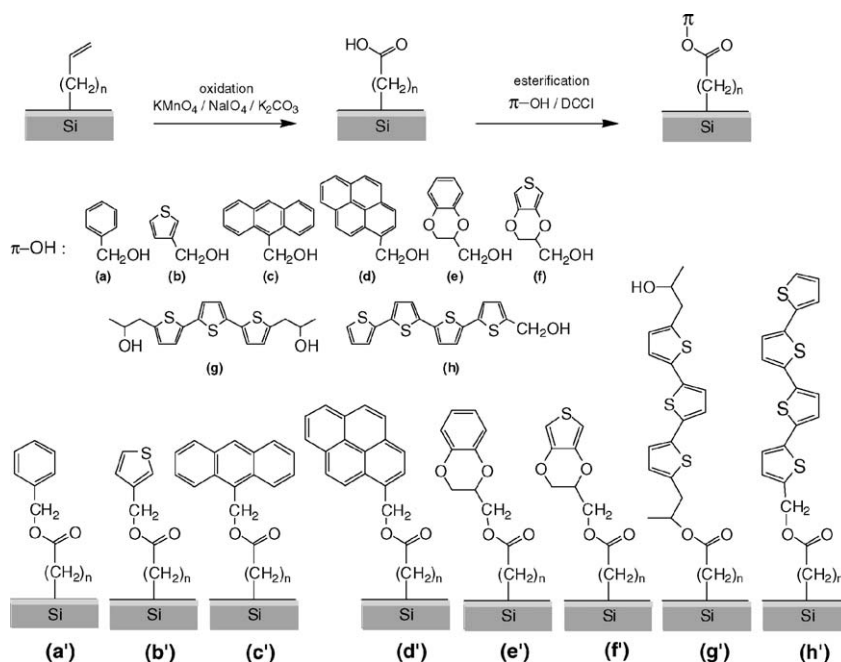


Fig. 24. The chemical synthesis of σ - π molecular diode using sequential self-assembly process. Chemical structures of π -alcohols used to functionalize the SAMs are: (a) benzyl alcohol, (b) 3-thiophenemethanol, (c) 9-anthracenemethanol, (d) 1-pyrenemethanol, (e) 3,4-ethylenedioxybenzene methanol (EDBM), (f) 3,4-ethylenedioxythiophene methanol (EDTM), (g) bis(2-hydroxypropyl)terthiophene (3T), and (h) hydroxymethyl quaterthiophene (4T). The schematic structures (a')–(h') correspond to σ - π molecular diodes made using π -alcohols (a)–(h), respectively.

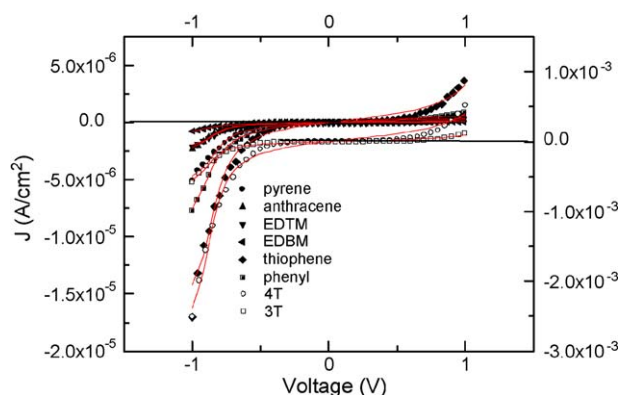


Fig. 25. Typical current density–voltage characteristics of the Si/ σ - π /Al junctions: HETS/phenyl (■); HETS/pyrene (●); HETS/thiophene (◆); HETS/anthracene (▲); HETS/EDTM (▼); HETS/EDBM (◄); OETS/3T (□) and OETS/4T (○). Left scale = HETS-based junctions; right scale = OETS-based junctions. Solid lines are fits by Eq. (10).

6.1.3. Rectifying characteristics

To fabricate diode using σ - π monolayers, Al counterelectrodes (10^{-4} cm² area and 10 nm thick) are deposited by an e-beam evaporator, as discussed in Section 4. Aluminum is chosen to avoid any rectification effect coming from the difference between the work functions of the two electrodes (4.2 eV for Al and 4.1 eV for n-type Si, electron affinity in that latter case). This is because, as discussed in Section 5, a largest current is obtained when a positive bias is applied to the electrode with the smallest work function.

Fig. 25 shows typical J - V curves for several π -terminated SAMs made with HETS as the alkyl spacer. In all cases, we measured a higher current density at -1 V than at 1 V. We observed a similar rectifying behavior for the SAMs based on the other alkyl chains (OETS and TETS) with similar π moieties at the end. We did not observe this rectification behavior when measuring the current through a monolayer without π group, i.e. the J - V curves for the OETS, TETS and HETS SAMs are symmetric. The electrical properties for various σ - π monolayers are presented in Table 3. For every π -functionalized monolayer,

a rectification ratio (RR) is defined as a ratio of current density at -1 V (in absolute value) and the current density at 1 V ($RR = |J_{-1V}|/|J_{1V}|$). The average values of RR are in the range 3–13 for the functionalized monolayers. The best RR value of 37 has been obtained for the OETS/thiophene monolayer. Neither a significant variation of RR with the chemical nature of the end-groups nor any correlation with the alkyl spacer length has been observed.

It has been demonstrated that the rectification behavior of these σ - π SAMs is due to the resonant tunneling through the HOMO of the π group [33]. The rectification effect arises for a negative bias applied on the Al electrode because the energy difference between the Si Fermi energy (pinned at the conduction band—CB—in the degenerated Si) and the HOMO (π orbital) is lower than that with the LUMO (π^* orbital). If we assume that the π -end group is almost at the Al electrode potential (since this group is at a close contact with the electrode) and that a large part of the potential is dropped in the alkyl chains, a lower threshold (in absolute value) is required to have a resonance between the Si CB and the HOMO when applying a negative bias on the metal electrode than between the Si CB and the LUMO for a positive bias. To determine the experimental position of the HOMO level, the J - V curves were fitted by a one-level model (i.e. a model in which the conduction is dominated by charge transport through a single energy level located at energy E_0 from the electrode Fermi energies). As discussed above, we assume here a resonant effect through the HOMO, then $E_0 < 0$, and the current density is given by [36,150],

$$J = \frac{2J_0}{\pi} \{ \tan^{-1}[\theta(|E_0| + \eta eV)] - \tan^{-1}[\theta(|E_0| - (1 - \eta)eV)] \} \quad (10)$$

where V is the applied potential on the metal electrode (Si is grounded), e is the electron charge, η is the fraction of the potential on the π moiety (i.e. the potential seen by the center of gravity of the π moiety), J_0 is the saturation current and θ is an electrode/molecule coupling parameter. The η value was estimated

Table 3

Average rectification ratio ($RR = J(-1\text{ V})/J(+1\text{ V})$), position of HOMO level relative to the Si-CB (E_0), coupling parameter (θ), theoretical HOMO and LUMO levels (obtained from self-consistent tight-binding (SC-TB) calculations, zero energy is the top of the Si VB, nc = non calculated) and molecular diode threshold voltage (V_T) for the various π -end groups

π -Group	RR	E_0 (eV)	θ (eV ⁻¹)	HOMO (eV)	LUMO (eV)	V_T (V)
Benzene	4.8 \pm 3.3 ^a	0.82 \pm 0.16	5.0 \pm 2.9	0.1	4.77	-0.64 \pm 0.07
Thiophene	13.3 \pm 13 ^b 2.7 \pm 1.4 ^a	0.80 \pm 0.14	7.5 \pm 2.8	0.44	3.87	-0.65 \pm 0.07
EDBM	4.7 \pm 2.9 ^a	0.75 \pm 0.03	8.5 \pm 0.5	nc	nc	-0.68 \pm 0.01
EDTM	6.7 \pm 2 ^a	0.73 \pm 0.03	7.4 \pm 2.7	nc	nc	-0.68 \pm 0.04
Pyrene	2.2 \pm 0.9 ^c 9.4 \pm 3.8 ^a	0.71 \pm 0.04	10.1 \pm 1.5	0.93	3.1	-0.68 \pm 0.02
Anthracene	8.1 \pm 2.9 ^a	0.75 \pm 0.09	10.4 \pm 1.2	1.1	3.2	-0.7 \pm 0.02
3T	3.6 \pm 1.4 ^b	0.81 \pm 0.1	8.6 \pm 1.6	1.1	3.05	-0.68 \pm 0.05
4T	4.6 \pm 0.2 ^b	0.77 \pm 0.07	9.2 \pm 0.3	nc	nc	-0.7 \pm 0.02

^a Alkyl chain = HETS.

^b Alkyl chain = OETS.

^c Alkyl chain = TETS.

using a simple dielectric model where the σ and π parts of the SAM have a thickness d_σ and d_π and a dielectric constant ε_σ and ε_π , respectively [35,151]

$$\eta = 1 - \frac{1}{2} \frac{1}{1 + (\varepsilon_\pi d_\sigma)/(\varepsilon_\sigma d_\pi)} \quad (11)$$

The SAM thicknesses were determined from ellipsometry measurements before and after the esterification of the π end-group. The dielectric constants of the thiophene, the phenyl and the alkyl chains are almost similar [152], so Eq. (11) reduces to $\eta = (d_\sigma + 0.5d_\pi)/(d_\sigma + d_\pi)$, which simply represents the relative position of the center of gravity of the π moiety measured from the Si substrate. Typical values are ~ 0.83 , ~ 0.87 and ~ 0.9 for the SAMs based on OETS, TETS and HETS, respectively. The solid lines in Fig. 25 are the best fits obtained using Eq. (10). The fitted parameters E_0 and θ are summarized in Table 3. It is observed that E_0 does not depend on the alkyl chain length. Also, the threshold voltage V_T , which is defined as the intercept between a linear fit of the current at high negative voltages and the zero current y-axis, does not depend on the nature of the π group. These observations warrant further theoretical as well as experimental investigations on the electronic transport in such molecular diodes.

6.2. Molecular resonant tunnel diode (MRTD)

6.2.1. Concept of MRTD

Conceptually the resonant tunnel diode consists of a double barrier heterostructure with barrier thickness of only few mono layers [1]. Based on this concept a design of molecular resonant tunnel diode (MRTD) is presented in Fig. 26(a). It essentially consists of a σ – π – σ self assembled mono layer on Si substrate. The two σ chains act as two tunnel barriers. The J – V behavior for such a σ – π – σ SAM, shown schematically in Fig. 26(b), is expected to exhibit a negative differential resistance (NDR), which arises due to a resonant tunneling mechanism. The schematic illustrations of simplified energy band diagrams that explain the charge transport mechanism in MRTD are shown in Fig. 26(c). In equilibrium, i.e. for $V=0$, the Fermi level, E_F ,

of Al lies with respect to the conduction band (CB) of the silicon. For simplicity, the band bending of Si at the interface is not shown. Also the HOMO and LUMO of σ molecules are not shown as the HOMO–LUMO gap for these molecules is much larger than that of π molecule. Under an increasing applied bias, i.e. $V>0$, the current, largely due to the non-resonant tunneling mechanism, increases. At a critical applied bias, V_R , the potential of the sample aligns with the LUMO, leading to resonant tunneling and a peak in the conduction. At a bias slightly higher than this critical value, i.e. $V>V_R$, conduction electrons move off resonance and the current reduces, which leads to a NDR.

6.2.2. Synthesis and characteristics of MRTD

As shown in Fig. 27, the σ – π – σ MRTD can be synthesized using two different processes [37]. In the first chemical process, see Fig. 27(a), the synthesis is made in five steps, i.e. silanization with vinyl terminated trichlorosilane, oxidation, esterification, demethylation, and repeated silanization with aliphatic trichlorosilane. The first three steps are same as those described for the synthesis of molecular σ – π diodes on Si surface. In the fourth step, i.e. demethylation, the end $-\text{OCH}_3$ group of σ – π molecules is replaced by OH group by reacting with BBr_3 . The terminating $-\text{OH}$ group then can be utilized for grafting another alkane chain by silanization process. In the other chemical process, as shown in Fig. 27(b), σ – π – σ MRTD, can be synthesized in just three steps, i.e. silanization, oxidation and esterification in the presence of σ – π alcohols. The J – V characteristics of these σ – π – σ MRTDs exhibited a very faint NDR effect, with ratio $J_{\text{peak}}/J_{\text{valley}}$ being only ~ 1.01 . The poor electrical characteristics are attributed to the very low yields of the formation of σ – π – σ SAMs. While the synthetic routes discussed above are well established, low yield of the reaction may lead to other chemical byproducts, which are likely to hamper the device characteristics.

According to the mechanism of NDR described in Fig. 26(c), in principle a single π -molecule chemisorbed on Si should be sufficient to act as MRTD. The most outstanding results on NDR have been observed through individual organic molecules, namely, styrene and 2,2,6,6-tetramethyl-

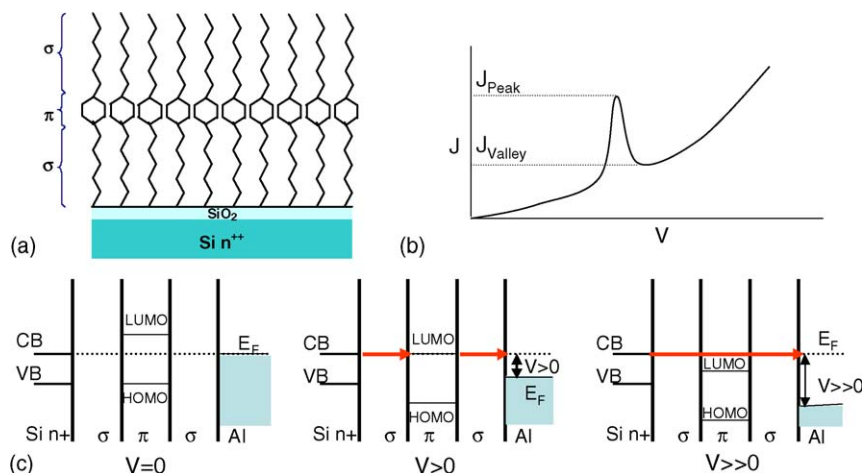


Fig. 26. Schematic diagram showing (a) concept, (b) characteristic J – V and (c) the mechanism of the occurrence of a negative differential resistance in a σ – π – σ SAM based MRTD (see text for the discussion).

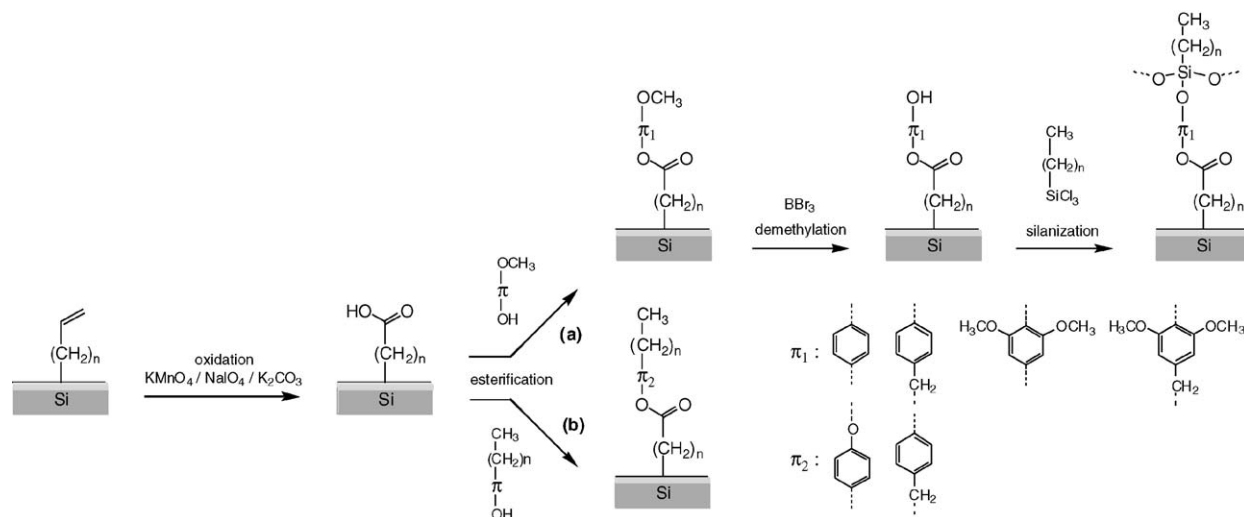


Fig. 27. Chemical synthesis process of σ - π - σ MRTD's in (a) five- and (b) three-steps.

1-piperidinyloxy (TEMPO), deposited on degenerately doped Si (100) 2×1 reconstructed surfaces using ultrahigh vacuum STM [48]. For styrene molecules on *n*-type Si (100), NDR is observed only for negative sample bias, while positive sample bias leads to electron stimulated desorption. For 2,2,6,6-tetramethyl-1-piperidinyloxy molecules, electron stimulated desorption was not observed at either bias polarity. In this case, NDR has been observed only for negative sample bias on *n*-type Si (100) and for positive sample bias on *p*-type Si (100). This unique behavior is consistent with a resonant tunneling mechanism between the bulk silicon band structure and the discrete orbitals of the adsorbed molecule, and opens new possibilities for silicon-based molecular electronic devices.

6.3. Molecular memories

The redox-active molecules, such as, metallocene, porphyrin, and triple-decker sandwich coordination compounds have been found to act as charge storage elements [153–155]. These molecules can be attached to device grade Si by self-assembly process, see Fig. 28. The molecular memory works on the

principle of charging or discharging of the molecules into different chemically reduced or oxidized (redox) states. Oxidation is equivalent to writing a bit of information, while reduction equates to erasing or destructively reading out that bit.

It has been demonstrated that porphyrins molecules (i) offer the possibility of multibit storage at relatively low potentials (below about 1.6 V), (ii) can undergo trillions of write/read cycles, (iii) exhibit charge-retention times that are long (minutes) compared with those of the semiconductor elements in dynamic random access devices (tens of milliseconds) and, (iv) are extremely stable under harsh conditions (e.g. monolayer of porphyrin molecules covalently attached to a silicon substrate are stable when subjected to temperatures of 400 °C for half an hour) and, therefore meet the processing and operating challenges required for use in semiconducting devices [154,155]. It is thus anticipated that the first generation of molecular devices will be hybrid designs where molecules are integrated with semiconductors. However, further investigations on the search of other types of redox-active molecules and, understanding the factors that control parameters, such as, electron transfer rate, which limits write/read times, and charge retention time, which determines refresh rates, are needed.

6.4. Molecular transistors

Field effect transistors are three-terminal devices. The concept of a self-assembled monolayer field-effect transistor [SAM-FET] is schematically shown in Fig. 29. The source (S) and drain (D) electrodes, separated by a distance L , are deposited on semiconducting channel made from π moieties. The alkyl chains of length (t) act as gate dielectric (G). FETs are based on a gate field modulating the conductance of the semiconducting channel to turn the device “off” and “on.” Unfortunately, the first report on SAMFET [156–158], containing monolayers of 1,1'-biphenyl-4,4'-dithiol has been found fraudulent [159]. Recently, the chemical and physical requirements necessary for the future successful design and fabrication of SAMFETs have been analyzed by Kagan et al. [160]. A theoretical analysis using electron

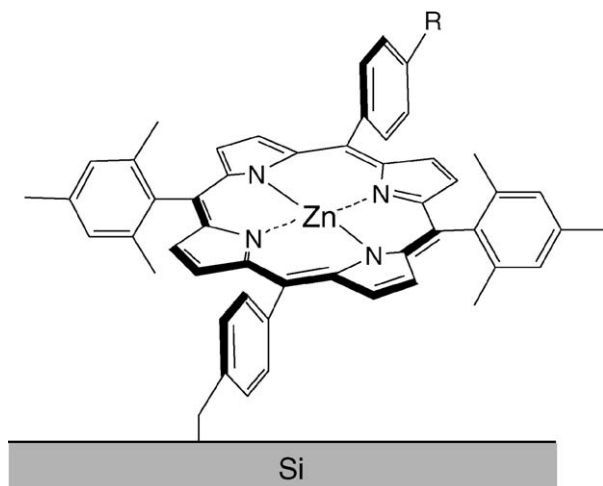


Fig. 28. Structure of a charge storage porphyrin molecule grafted on Si.

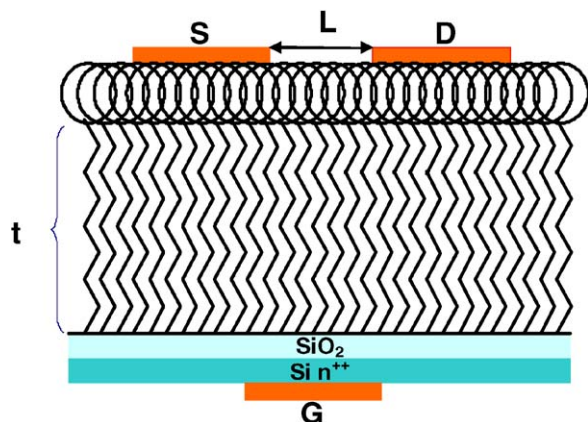


Fig. 29. Schematic showing a concept of self-assembled monolayer field effect transistor (SAMFET) based on a σ - π molecule. No experimental demonstration of such a SAMFET has been made so far.

tunneling and device electrostatics place $L > 2.5$ –3 nm and minimum gate dielectric thickness $t = L/1.5$ for such devices [160].

On experimental front two major independent works have been reported

- (i) *Dielectric behavior of alkyl chains.* The suitability of these alkyl chains have been demonstrated for the fabrication of sexithiophene [36,39] or pentacene [136] based Organic thin film transistors (OTFTs).
- (ii) *OH- functionalized tetracene self-assembled monolayer acting as an active channel of the transistor.* A transistor behavior has been observed when OH- functionalized tetracene self-assembled monolayer was deposited on pre-fabricated transistor structures [161]. A layer of aluminum oxide (~ 5 nm) was utilized to act both as a dielectric layer and also as a primer for the assembly of the monolayer.

Probably it is just a matter of time when a chemist would graft OH- functionalized tetracene type monolayer semiconducting channels directly on the alkyl chain dielectrics to fabricate true molecular transistors.

7. Concluding remarks

The self-assembly of organic monolayers on Si substrates continues to be of great interest in our quest for achieving nanometer scale electronic devices, i.e. molecular electronics, and/or hybrid electronics. A certain amount of progress has already been made in this direction, but there are several challenges that must be addressed to make significant progress in molecular electronics. These include:

- (i) Organic molecules used for deposition of SAMs should be of very high purity. Otherwise, the impurities would dominate the electrical properties of the device.
- (ii) Chemical yield of the functional SAMs, e.g. σ - π (for molecular diodes), σ - π - σ (for resonant tunnel diode), etc. need to be improved in order to obtain reliable device characteristics. At present, multiple step chemical processes are being utilized for synthesis of functional SAMs, however

novel synthesis routes need to be explored to minimize the steps and to improve the yield.

- (iii) The fabrication of metal counterelectrode that does not diffuse into SAM and create short-circuits need to be mastered. Soft-lithography is good option, but it demands a surface group (e.g. -SH) that can react with metal (e.g. Au). Synthesis of functional SAMs with such a surface group would not only lead to the reliable device characteristics but also allow the investigation of the origin of charge transport in them.
- (iv) Many SAMs with new mechanisms, such as, σ - π system with large in-plane conductivity for molecular transistors, molecular systems showing conformational changes with reduction-oxidation for attaining switching characteristics in molecular devices, etc. are need to be envisioned and synthetically engineered.

Acknowledgements

This work was supported by Indo-French Centre for the Promotion of Advanced Research (IFCPAR) through Project No. 3000-IT-I, and by the “Institut de Recherche sur les Composants logiciels et matériels pour l’Informatique et la Communication Avancée” (IRCICA) and by the “ministère de la recherche” through the “AC nanosciences” program.

References

- [1] S.M. Sze, Semiconductor Devices: Physics and Technology, John Wiley & Sons, New York, 2002.
- [2] G.E. Moore, Electronics 38 (1965) 1.
- [3] B. Mann, H. Kuhn, J. Appl. Phys. 42 (1971) 4398.
- [4] E.E. Polymeropoulos, J. Sagiv, J. Chem. Phys. 69 (1978) 1836.
- [5] L. Netzer, J. Sagiv, J. Am. Chem. Soc. 105 (1983) 674.
- [6] I. Langmuir, Trans. Faraday Soc. 15 (1920) 62.
- [7] A. Ulman, An Introduction to Ultrathin Organic Films From Langmuir-Blogett to Self-Assembly, Academic Press, 1991.
- [8] A. Aviram, M.A. Ratner, Chem. Phys. Lett. 29 (1974) 277.
- [9] F.L. Carter, R.E. Siatkowski, H. Wohltjen (Eds.), Molecular Electronic Devices: Proc. 3rd Int. Symp. on Molecular Electronic Devices, North-Holland, New York, 1989.
- [10] G. Binnig, H. Rohrer, C. Gerber, E. Weibel, Phys. Rev. Lett. 49 (1982) 57.
- [11] G. Binnig, H. Rohrer, Rev. Mod. Phys. 59 (1987) 615.
- [12] M.A. Reed, C. Zhou, C.J. Miller, T.P. Burgin, J.M. Tour, Science 278 (1997) 252.
- [13] H.B. Weber, J. Reichert, F. Weigend, R. Ochs, D. Beckmann, M. Mayor, R. Ahlrichs, H. von Löhneysen, Chem. Phys. 281 (2002) 113.
- [14] C. Kergueris, I.P. Bourgoin, S. Palacin, D. Esteve, C. Urbina, M. Magoga, C. Joachim, Phys. Rev. B 59 (1999) 12505.
- [15] J.G. Kushmenck, D.B. Holt, J.C. Yang, J. Naciri, M.H. Moore, R. Shashidhar, Phys. Rev. Lett. 89 (2002) 086802.
- [16] A. Bezryadin, C. Dekker, G. Schmid, Appl. Phys. Lett. 71 (1997) 1273.
- [17] B. Xu, N.J. Tao, Science 301 (2003) 1221.
- [18] D.J. Wold, C.D. Frisbie, J. Am. Chem. Soc. 123 (2001) 5549.
- [19] X.D. Cui, X. Zarate, J. Tomfohr, O.F. Sankey, A. Primak, A.L. Moore, T.A. Moore, D. Gust, G. Harris, S.M. Lindsay, Nanotechnology 13 (2002) 5.
- [20] X.D. Cui, A. Primak, X. Zarate, J. Tomfohr, O.F. Sankey, A.L. Moore, T.A. Moore, D. Gust, L.A. Nagahara, S.M. Lindsay, J. Phys. Chem. B 106 (2002) 8609.

- [21] J. Chen, M.A. Reed, A.M. Rawlett, J.M. Tour, *Science* 286 (1999) 1550.
- [22] C. Zhou, M.R. Deshpande, M.A. Reed, L. Jones II, J.M. Tour, *Appl. Phys. Lett.* 71 (1997) 611.
- [23] K.S. Ralls, R.A. Buhrman, R.C. Tiberio, *Appl. Phys. Lett.* 55 (1989) 2459.
- [24] A. Salomon, D. Cahen, S.M. Lindsay, J. Tomfohr, V.B. Engelkes, C.D. Frisbie, *Adv. Mater.* 15 (2003) 1881.
- [25] R.G. Nuzzo, D.L. Allara, *J. Am. Chem. Soc.* 105 (1983) 4481.
- [26] A. Ulman, *Chem. Rev.* 96 (1996) 1533.
- [27] L.H. Dubois, R.G. Nuzzo, *Annu. Rev. Phys. Chem.* 43 (1992) 437.
- [28] F. Schreiber, *Prog. Surf. Sci.* 65 (2000) 151.
- [29] F. Schreiber, *J. Phys.: Condens. Matter* 16 (2004) R881.
- [30] J.C. Love, L.A. Estroff, J.K. Kriebel, R.G. Nuzzo, G.M. Whitesides, *Chem. Rev.* 105 (2005) 1103.
- [31] W.C. Bigelow, D.I. Pickett, W.A. Zisman, *J. Colloid Sci.* 1 (1946) 513.
- [32] R. Maoz, J. Sagiv, *J. Colloid Interf. Sci.* 100 (1984) 465.
- [33] D.K. Aswal, S. Lenfant, D. Guerin, J.V. Yakhmi, D. Vuillaume, *Small* 1 (2005) 725.
- [34] C. Miramond, D. Vuillaume, *J. Appl. Phys.* 96 (2004) 1529.
- [35] S. Lenfant, C. Krzeminski, C. Delerue, G. Aallan, D. Vuillaume, *Nano Lett.* 3 (2003) 741.
- [36] D. Vuillaume, *J. Nanosci. Nanotechnol.* 2 (2002) 267.
- [37] S. Lenfant, Ph.D. Thesis, Organic self-assembled monolayers for molecular diodes, 2001. University of Science and Technology, Lille, France.
- [38] S. Kar, C. Miramond, D. Vuillaume, *Appl. Phys. Lett.* 78 (2001) 1288.
- [39] J. Collet, O. Tharaud, A. Chapoton, D. Vuillaume, *Appl. Phys. Lett.* 76 (2000) 1941.
- [40] L. Breuil, Ph.D. Thesis, 2000. University of Science and Technology, Lille, France.
- [41] J. Collet, S. Lenfant, D. Vuillaume, O. Bouloussa, F. Rondelez, J.M. Gay, K. Kham, C. Chevrot, *Appl. Phys. Lett.* 76 (2000) 1339.
- [42] J. Collet, D. Vuillaume, *Appl. Phys. Lett.* 78 (1998) 2681.
- [43] D. Vuillaume, C. Boudas, J. Collet, G. Allan, C. Delerue, *Phys. Rev. B* 58 (1998) 16491.
- [44] D. Vuillaume, *Mater. Res. Soc. Proc.* 446 (1997) 79.
- [45] C. Boudas, J. Davindovits, F. Rondelez, D. Vuillaume, *Phys. Rev. Lett.* 76 (1996) 4797.
- [46] D. Vuillaume, C. Boudas, J. Collet, J. Davindovits, F. Rondelez, *Appl. Phys. Lett.* 69 (1996) 1646.
- [47] P. Fontaine, D. Goguenheim, D. Deresmes, D. Vuillaume, M. Garret, F. Rondelez, *Appl. Phys. Lett.* 62 (1993) 2256.
- [48] N.P. Guisinger, M.E. Greene, R. Basu, A.S. Baluch, M.C. Hersam, *Nano Lett.* 4 (2004) 55.
- [49] S. Wolf, R. Tauber, *Silicon Processing*, Vol. 1, Lattice Press, CA, 1986.
- [50] W. Kern, D.A. Puotinen, *Cleaning solutions based on hydrogen peroxide for use in silicon semiconductor technology*, RCA Rev. (1970) 187.
- [51] J.B. Brzoska, I.B. Azouz, F. Rondelez, *Langmuir* 10 (1994) 4367.
- [52] S.R. Wasserman, Y.-T. Tao, G.M. Whitesides, *Langmuir* 5 (1989) 1074.
- [53] N. Tillman, A. Ulman, J.S. Schildkraut, T.L. Penner, *J. Am. Chem. Soc.* 110 (1988) 6136.
- [54] S. Petitdidier, V. Bertagna, N. Rochat, D. Rouchon, P. Besson, R. Erre, M. Chemla, *Thin Solid Films* 476 (2005) 51.
- [55] K. Choi, T.-J. Eom, C. Lee, *Thin Solid Films* 435 (2003) 227.
- [56] P.J. Hergenrother, K.M. Depew, S.L. Schreiber, *J. Am. Chem. Soc.* 122 (2000) 7849.
- [57] M.G.L. Petrucci, A.K. Kakkar, *Chem. Mater.* 11 (1999) 269.
- [58] R.C. Major, X.-Y. Zhu, *Langmuir* 17 (2001) 5576.
- [59] N. Rozlosnik, M.C. Gerstenberg, N.B. Larsen, *Langmuir* 19 (2003) 1182.
- [60] E. Pavlovic, A.P. Quist, U. Gelius, S. Oscarsson, *J. Colloid Interf. Sci.* 254 (2002) 200.
- [61] G. Ledung, M. Bergkvist, A.P. Quist, U. Gelius, J. Carlsson, S. Oscarsson, *Langmuir* 17 (2001) 6056.
- [62] J.M. Buriak, *Chem. Rev.* 102 (2002) 1271.
- [63] S.F. Bent, *Surf. Sci.* 500 (2002) 879.
- [64] G.S. Higashi, Y.J. Chabal, G.W. Trucks, K. Raghavachari, *Appl. Phys. Lett.* 56 (1990) 656.
- [65] G.S. Higashi, R.S. Becker, Y.J. Chabal, A.J. Becker, *Appl. Phys. Lett.* 58 (1991) 1656.
- [66] A. Bansal, X. Li, I. Lauermaun, N.S. Lewis, *J. Am. Chem. Soc.* 118 (1996) 7225.
- [67] A. Bansal, X. Li, S.I. Yi, W.H. Weinberg, N.S. Lewis, *J. Phys. Chem. B* 105 (2001) 10266.
- [68] X.-Y. Zhu, V. Boiadjev, J.A. Mulder, R.P. Hsung, R.C. Major, *Langmuir* 16 (2000) 6766.
- [69] B.J. Eves, G.P. Lopinski, *Surf. Sci.* 579 (2005) L89.
- [70] D. Narducci, L. Pedemonte, G. Bracco, *Appl. Surf. Sci.* 212 (2003) 649.
- [71] L. Pedemonte, G. Bracco, A. Relini, R. Rolandi, D. Narducci, *Appl. Surf. Sci.* 212 (2003) 595.
- [72] J.M. Lauerhaas, M.J. Sailor, *Science* 261 (1993) 1567.
- [73] J.M. Lauerhaas, M.J. Sailor, *Mater. Res. Soc. Symp. Proc.* 298 (1993) 259.
- [74] V.T. Joy, D. Mandler, *Chem. Phys. Chem.* 3 (2002) 973.
- [75] C.B. Duke, *Chem. Rev.* 96 (1996) 1237.
- [76] H.N. Waltenberg, J.T. Yates Jr., *Chem. Rev.* 95 (1995) 1589.
- [77] M.R. Linford, C.E.D. Chidsey, *J. Am. Chem. Soc.* 115 (1993) 12631.
- [78] M.R. Linford, P. Fenter, P.M. Eisenberger, C.E.D. Chidsey, *J. Am. Chem. Soc.* 117 (1995) 3145.
- [79] J.A. Labinger, in: B.M. Trost, I. Fleming (Eds.), *Comprehensive Organic Synthesis*, Vol. 8, Pergamon, New York, 1991, p. 699.
- [80] M.M. Sung, J. Kluth, O.W. Yauw, R. Maboudian, *Langmuir* 13 (1997) 6164.
- [81] J. Terry, M.R. Linford, C. Wigren, R. Cao, P. Pianetta, C.E.D. Chidsey, *Appl. Phys. Lett.* 71 (1997) 1056.
- [82] R.L. Cicero, M.R. Linford, C.E.D. Chidsey, *Langmuir* 16 (2000) 5688.
- [83] C.H. de Villeneuve, J. Pinson, M.C. Bernard, P. Allongue, *J. Phys. Chem. B* 101 (1997) 2415.
- [84] J.H. Song, M.J. Sailor, *J. Am. Chem. Soc.* 120 (1998) 2376.
- [85] N.Y. Kim, P.E. Laibinis, *J. Am. Chem. Soc.* 121 (1999) 7162.
- [86] R. Konecny, D.J. Doren, *Surf. Sci.* 417 (1998) 169.
- [87] Q. Liu, R.J. Hoffmann, *J. Am. Chem. Soc.* 117 (1995) 4082.
- [88] C. Huang, W. Widdra, X.S. Wang, W.H. Weinberg, *J. Vac. Sci. Technol. A* 11 (1993) 2250.
- [89] R. Terborg, P. Baumgartel, R. Lindsay, O. Schaff, T. Giessel, J.T. Hoeft, M. Polcik, R.L. Toomes, S. Kulkarni, A.M. Bradshaw, D.P. Woodruff, *Phys. Rev. B* 61 (2000) 16697.
- [90] R.M. Nyffenegger, R.M. Penner, *Chem. Rev.* 97 (1997) 1195.
- [91] G.C. Abeln, S.Y. Lee, J.W. Lyding, D.S. Thompson, J.S. Moore, *Appl. Phys. Lett.* 70 (1997) 2747.
- [92] M.C. Petty, in: G. Roberts (Ed.), *Langmuir-Blodgett Films*, Plenum Press, New York, 1990.
- [93] R.M.A. Azzam, N.M. Bashara, *Ellipsometry and Polarized Light*, North Holland, Amsterdam, 1977.
- [94] B. Rothenhauser, C. Duschl, W. Knoll, *Thin Solid Films* 150 (1988) 323.
- [95] M. Pomerantz, A. Segmuller, *Thin Solid Films* 68 (1980) 33.
- [96] T. Nakagiri, K. Sakai, A. Lida, T. Ishikawa, T. Matsushita, *Thin Solid Films* 133 (1985) 219.
- [97] D.L. Allara, A.N. Parikh, F. Rondelez, *Langmuir* 11 (1995) 2357.
- [98] A.B. Sieval, V. Vleeming, H. Zuilhof, E.J.R. Sudholter, *Langmuir* 15 (1999) 8288.
- [99] J. Cheng, D.B. Robinson, R.L. Cicero, T. Eberspacher, C.J. Barrelet, C.E.D. Chidsey, *J. Phys. Chem. B* 105 (2001) 10900.
- [100] A.B. Sieval, B. van den Hout, H. Zuilhof, E.J.R. Sudholter, *Langmuir* 17 (2001) 2172.
- [101] M.D. Porter, T.B. Bright, D.L. Allara, C.E.D. Chidsey, *J. Am. Chem. Soc.* 109 (1987) 3559.
- [102] V.K. Srivastava, A.R. Verma, *Solid State Commun.* 4 (1966) 367.
- [103] A. Bonnerot, P.A. Chollet, H. Frisby, M. Hoclet, *Chem. Phys.* 97 (1985) 365.

- [104] L. Valkova, A. Menelle, N. Borovkov, V. Erokhin, M. Pisani, F. Ciuchi, F. Carsughi, F. Spinozzi, M. Pergolini, R. Padke, S. Bernstorff, F. Rustichelli, *J. Appl. Cryst.* 36 (2003) 758.
- [105] R. Becker, M.R. Ashton, T.S. Jones, N.V. Richardson, H. Sotobayashi, *J. Phys.: Condens. Matter* 3 (1991) S29.
- [106] T. Takenaka, *Chem. Phys. Lett.* 55 (1978) 515.
- [107] A. Fujimori, M. Ishitsuka, H. Nakahara, E. Ito, M. Hara, K. Kanai, H. Ishii, Y. Ouchi, K. Seki, *J. Poly. Sci. B.* 42 (2004) 2329.
- [108] A.Y. Fadeev, T.J. McCarthy, *Langmuir* 16 (2000) 7268.
- [109] H.H.J. Persson, W.R. Caseri, U.W. Suter, *Langmuir* 17 (2001) 3643.
- [110] G.J. Kluth, M.M. Sung, R. Maboudian, *Langmuir* 13 (1997) 3775.
- [111] H. Ahn, M. Kim, D.J. Sandman, J.E. Whitten, *Langmuir* 19 (2003) 5303.
- [112] A.C. Friedli, R.D. Roberts, C.S. Dulcey, A.R. Hsu, S.W. McElvany, J.M. Calvert, *Langmuir* 20 (2004) 4295.
- [113] J.J. Senkevich, C.J. Mitchell, G.-R. Yang, T.-M. Lu, *Langmuir* 18 (2002) 1587.
- [114] N. Balachander, C.N. Sukenik, *Langmuir* 6 (1990) 1621.
- [115] M.V. Baker, J.D. Watling, *Langmuir* 13 (1997) 2027.
- [116] R. Sfez, L. De-Zhong, I. Turyan, D. Mandler, S. Yitzchaik, *Langmuir* 17 (2001) 2556.
- [117] P.E. Laibinis, G.M. Whitesides, *J. Am. Chem. Soc.* 114 (1992) 1990.
- [118] A.G. Frutos, J.M. Brockman, R.M. Corn, *Langmuir* 16 (2000) 2192.
- [119] M.-T. Lee, G.S. Ferguson, *Langmuir* 17 (2001) 762.
- [120] V.V. Tsukruk, L.M. Lander, W.J. Bnttain, *Langmuir* 10 (1994) 996.
- [121] Y.-S. Shon, K.F. Kelly, N.J. Halas, T.R. Lee, *Langmuir* 15 (1999) 5329.
- [122] W. Zisman, in: F.M. Fowkes (Ed.), *Contact Angle, Wettability, and Adhesion*, Vol. 43, American Chemical Society, Washington, 1964, p. 1.
- [123] K. Kojio, S. Ge, A. Takahara, T. Kajiyama, *Langmuir* 14 (1998) 971.
- [124] I. Doudevski, W.A. Hayes, D.K. Schwartz, *Phys. Rev. Lett.* 81 (1998) 4927.
- [125] D.K. Schwartz, S. Steinberg, J. Israelachvili, J.A.N. Zasadzinski, *Phys. Rev. Lett.* 69 (1992) 3354.
- [126] K. Bierbaum, M. Grunze, A.A. Baski, L.F. Chi, W. Schrepp, H. Fuchs, *Langmuir* 11 (1995) 2143.
- [127] E. Sabatani, I. Rubinstein, *J. Phys. Chem.* 91 (1987) 6663.
- [128] H.O. Finklea, Self assembled monolayers on electrodes, in: A. Robert (Ed.), *Meyers Encyclopedia of Analytical Chemistry*, John Wiley & Sons Ltd, Chichester, 2000, ISBN 0471 97670 9.
- [129] D. Briggs, M.P. Seah, *Practical Surface Analysis by Auger and X-ray Photoelectron Spectroscopy*, Wiley, 1983.
- [130] Y. Selzer, A. Salomon, D. Cahen, *J. Phys. Chem. B* 106 (2002) 10432.
- [131] Y.-L. Liu, H.-Z. Yu, *Chem. Phys. Chem.* 19 (2002) 799.
- [132] R.M. Metzger, T. Xu, I.R. Peterson, *J. Phys. Chem. B* 105 (2001) 7280.
- [133] Y. Xia, G.M. Whitesides, *Angew. Chem. Int. Ed.* 37 (1998) 550.
- [134] S. Jeon, E. Menard, J.-U. Park, J. Maria, M. Meitel, J. Zaumseil, J.A. Rogers, *Adv. Mater.* 16 (2004) 1369.
- [135] C. Krzeminski, C. Delerue, G. Aallan, D. Vuillaume, R.M. Metzger, *Phys. Rev. B* 64 (2001) 085405.
- [136] M. Halik, H. Klauk, U. Zschieschang, G. Schmid, C. Dehm, M. Schütz, S. Maisch, F. Effenberger, M. Brunnbauer, F. Stellacci, *Nature* 431 (2004) 963.
- [137] P.C.W. Davies, D.S. Betts, *Quantum Mechanics*, Chapman & Hall, London, 1994.
- [138] J.G. Simmons, *J. Appl. Phys.* 34 (1963) 2581.
- [139] P. Hesto, in: G. Barbotin, A. Vapaille (Eds.), *Instabilities in Silicon Devices*, North Holland, Netherlands, 1986, p. 263.
- [140] D.R. Lide (Ed.), *CRC Handbook of Chemistry and Physics*, 74th ed., CRC Press, Boca Raton, 1993–1994, pp. 12–105.
- [141] J.M. Tomfohr, O.F. Sankey, *Phys. Rev. B* 65 (2002) 245105.
- [142] M. Lenzlinger, E.H. Snow, *J. Appl. Phys.* 40 (1969) 278.
- [143] Y. Selzer, A. Salomon, D. Cahen, *J. Am. Chem. Soc.* 124 (2002) 2886.
- [144] M. Porti, N. Nafria, X. Aymerich, A. Olbrich, B. Ebersberger, *J. Appl. Phys.* 91 (2002) 2071.
- [145] J. Zhou, K. Uosaki, *Appl. Phys. Lett.* 83 (2003) 2034.
- [146] M.L. Green, E.P. Gusev, R. Degraeve, E.L. Garfunkel, *J. Appl. Phys.* 90 (2001) 2057.
- [147] R.M. Metzger, *Chem. Rev.* 103 (2003) 3803.
- [148] R.M. Metzger, B. Chen, U. Höpfner, M.V. Lakshmikantham, D. Vuillaume, T. Kawai, X. Wu, H. Tachibana, T.V. Hughes, H. Sakurai, J.W. Baldwin, C. Hosch, M.P. Cava, L. Brehmer, G.J. Ashwell, *J. Am. Chem. Soc.* 119 (1997) 10455.
- [149] P.E. Kornilovitch, A.M. Bratkovsky, R.S. Williams, *Phys. Rev. B* 66 (2002) 165436.
- [150] L.E. Hall, J.R. Reimers, N.S. Hush, K. Silverbrook, *J. Chem. Phys.* 112 (2000) 1510.
- [151] D. Vuillaume, B. Chen, R.M. Metzger, *Langmuir* 15 (1999) 4011.
- [152] S. Budavari, *The Merck Index*, 12th ed., Merck & Co. Inc., Whitehouse Station, 1996.
- [153] W.G. Kuhr, A.R. Gallo, R.W. Manning, C.W. Rhodine, *MRS Bull.* November (2004) 838.
- [154] Z. Liu, A.A. Yasseri, J.S. Lindsey, D.F. Bocian, *Science* 302 (2003) 1543.
- [155] K.M. Roth, N. Dontha, R.B. Dabke, D.T. Gryko, C. Clausen, J.S. Lindsey, D.F. Bocian, W.G. Kuhr, *J. Vac. Sci. Technol. B* 18 (2000) 2359.
- [156] J.H. Schon, H. Meng, Z. Bao, *Nature* 413 (2001) 713.
- [157] J.H. Schon, H. Meng, Z. Bao, *Science* 294 (2001) 2138.
- [158] J.H. Schon, Z. Bao, *Appl. Phys. Lett.* 80 (2002) 847.
- [159] M.R. Beasley, S. Datta, H. Kogelnik, H. Kroemer, D. Monroe, Report of the Investigation Committee on the Possibility of Scientific Misconduct in the Work of Hendrik Schon and Coauthors, September 2002.
- [160] C.R. Kagan, A. Afzali, R. Martel, L.M. Gignac, P.M. Solomon, A.G. Schrott, B. Ek, *Nano Lett.* 3 (2003) 119.
- [161] G.S. Tulevski, Q. Miao, M. Fukuto, R. Abram, B. Ocko, R. Pindak, M.L. Steigerwald, C.R. Kagan, C. Nuckolls, *J. Am. Chem. Soc.* 126 (2004) 15048.